catalysts

MDPI

Review

Hierarchical Nanostructured Photocatalysts for CO_2 Photoreduction

Chaitanya Hiragond, Shahzad Ali, Saurav Sorcar and Su-Il In *

Department of Energy Science & Engineering, DGIST, 333 Techno Jungang-daero, Hyeonpung myeon, Dalseong-gun, Daegu 42988, Korea; chetan123@dgist.ac.kr (C.H.); shahzadali@dgist.ac.kr (S.A.); sorcar@dgist.ac.kr (S.S.)

* Correspondence: insuil@dgist.ac.kr; Tel.: +82-053-785-6438

Received: 31 March 2019; Accepted: 17 April 2019; Published: 19 April 2019

Abstract: Practical implementation of CO_2 photoreduction technologies requires low-cost, highly efficient, and robust photocatalysts. High surface area photocatalysts are notable in that they offer abundant active sites and enhanced light harvesting. Here we summarize the progress in CO_2 photoreduction with respect to synthesis and application of hierarchical nanostructured photocatalysts.

Keywords: hierarchical; nanostructure; photoreduction; photocatalytic; CO_2; solar fuels

1. Introduction

The deleterious environmental impacts of fossil fuel [1] combustion are now well recognized [2–12], making clear the critical need to develop renewable energy technologies. In this regard, the conversion of CO_2 into fuel has received considerable attention in the past few years [13–24]. The utilization of solar energy for conversion of CO_2 into hydrocarbon fuels, compatible with the current energy infrastructure, is an intriguing idea for solving both energy and pollution issues [25–43]. However, to date CO_2 photoreduction efficiencies, and the intrinsic stability of the photocatalysts, remain too low for commercial application [44–47].

When semiconductors are exposed to photons possessing energy equal to or higher than the band gap energy, electron–hole pairs are generated. Some of these photogenerated charges undergo redox reactions, while others simply recombine thus limiting photocatalytic efficiency [48]. In this regard, the design of an efficient, highly stable and cost-effective photocatalytic system is necessary for practical implementation. While a number of semiconductor photocatalysts have been extensively studied for CO_2 photoreduction, such as, for example, ZnO [49–51], TiO_2 [52–58], CdS [59–61], Fe_2O_3 [62–64], g-C_3N_4 [65–69], Cu_2O [70–72], and Bi_2WO_6 [73–75], their performance is not yet sufficient for practical implementation due to constraints such as band gap energy that is too large, high recombination rate, and cost. To overcome such difficulties band gap engineering of semiconductor photocatalysts through co-catalyst insertion, synthesis of different morphologies, heterojunction and Z-scheme construction are of ongoing interest [76]. Hierarchical nanostructured materials offer the opportunity for readily modifying crystal structure, band gap alignment, and composition [52,77–79]. The hierarchical materials are typically composed of low-dimensional sub-units arranged in a well-ordered manner [80]. Compared to bulk materials these complex hierarchical nanostructures possess high surface area, enable enhanced light harvesting, and have high CO_2 adsorption and activation properties that correspond to higher reaction rates and photocatalytic activity [81,82]. In this review we examine progress in the synthesis and application of different hierarchical CO_2 photoreduction photocatalysts, elucidating pathways by which higher performance might be achieved.

2. CO_2 Photoreduction Mechanism

CO_2 reduction begins with breaking of the O=C=O bond to form new carbon bonds [48]. Photocatalytic CO_2 reduction is considered a "proton-assisted multi-electron reduction process" involving different intermediate steps as indicated in Table 1, with intermediate products dependent upon the availability (density) of photogenerated electrons [83]. When a single electron is transferred to an adsorbed CO_2 molecule on the surface of a photocatalyst it results in an unstable $CO_2^{\bullet-}$ radical formation that has a redox potential of −1.90 V versus normal hydrogen electrode (NHE) as shown in Table 1, equation 1. The relative conduction band (CB) edges of most of semiconducting materials have lower reduction potential than that of $CO_2^{\bullet-}$ radical, therefore this reaction is unfeasible without a high over potential. The proton assisted transfer of multiple electrons is considered more favorable for CO_2 reduction reaction [48]. The as-produced $CO_2^{\bullet-}$ anion radical further counters with electrons (e^-) and protons (H^+), giving rise to different products such as CO, HCHO, HCOOH, CH_3OH and CH_4 depending upon their relative redox potential. When surface-absorbed CO_2 reacts with two protons and two electrons, it produces carbon monoxide (CO), with the possible formation of formic acid (HCOOH). Furthermore, the formaldehyde can be produced by reacting CO_2 with $4e^-$ and $4H^+$ ions. However, higher hydrocarbon like CH_4/CH_3OH can be produced by contributing 8/6 electrons and protons, respectively. One can tune the yield and selectivity of the product by manipulating factors like the band gap of the semiconductor, photo excited charge carriers, conductivity and engineering of surface morphology. This kind of engineering can also be helpful for production of higher hydrocarbon fuels from CO_2 photoreduction.

Table 1. The main products of CO_2 reduction with the corresponding reduction potentials (pH = 7).

Reaction	Product	E°_{redox}	Equation
$CO_2 + e^- \rightarrow CO_2^{\bullet-}$	$CO_2^{\bullet-}$ anion radical	−1.90 V	(1)
$CO_2 + 2H^+ + 2e^- \rightarrow HCOOH$	Formic acid	−0.61 V	(2)
$CO_2 + 2H^+ + 2e^- \rightarrow CO + H_2O$	Carbon monoxide	−0.53 V	(3)
$CO_2 + 4H^+ + 4e^- \rightarrow HCHO + H_2O$	Formaldehyde	−0.48 V	(4)
$CO_2 + 6H^+ + 6e^- \rightarrow CH_3OH + H_2O$	Methanol	−0.38 V	(5)
$CO_2 + 8H^+ + 8e^- \rightarrow CH_4 + 2H_2O$	Methane	−0.24 V	(6)
$2H^+ + 2e^- \rightarrow H_2$	Hydrogen	−0.41 V	(7)

3. Benefits of Hierarchical Nanostructures in Photocatalysis

Hierarchical nanostructures offer a promising avenue for achieving enhanced photocatalytic activity due to their special features as illustrated in Figure 1.

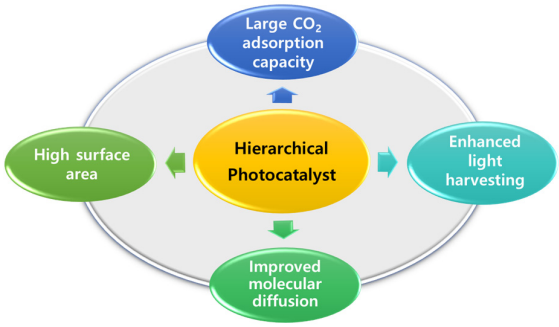

Figure 1. Important features of hierarchical nanostructures.

In heterogeneous photocatalysis it is recognized that high surface area corresponds to increased overall photocatalytic activity. Jiao et al., for example, reported that hollow and mesoporous TiO_2 shows improved CO_2 conversion into CH_4 as compared with solid, low surface area, TiO_2 crystals [84]. Xiao et al. fabricated Bi_2WO_6 nanosheets which displayed 58 times higher specific surface area

than that of bulk Bi_2WO_6 [85], 42.87 m^2 g^{-1} versus 0.73 m^2 g^{-1}. Such high specific surface area of hollow Bi_2WO_6 has greatly improved photocatalytic CO_2 reduction into CH_4. On the other hand, the carbon allotrope-based hierarchical materials reached 800–2800 m^2 g^{-1} specific surface area [76]. These studies imply a significant synergistic effect of high specific surface area of hierarchical nanostructures resulting in enhanced CO_2 adsorption and photoreduction. To achieve large CO_2 adsorption, various strategies have been successfully employed including: (i) augmentation of surface area, (ii) improvement in mass transfer, and (iii) expansion of the basic sites. Hierarchical materials with single/multicomponent mesoporous structures possess high CO_2 adsorption capacity due to their porous and hollow morphology. For instance, Pan et al. synthesized $LaPO_4$ hierarchical hollow spheres with enhanced photocatalytic CO_2 reduction activity and selectivity for CH_4 production was attributed to higher CO_2 adsorption ability [86]. Similarly, Fu et al. reported that O-doped g-C_3N_4 porous material having a higher CO_2 uptake ability than that of bulk g-C_3N_4, which resulted in enhanced photocatalytic CO_2 reduction [87]. It is well known that increased light-harvesting ability can greatly boost photocatalytic performance [88,89]. Hollow and mesoporous nanostructures, for example, have the ability to scatter light inside the pores hence improving light absorption efficiency. Recently Zhang et al. fabricated hierarchical CdS multi-cavity hollow nanoparticles that demonstrated high rates of CO_2 to CO conversion, a behavior attributed to the hollow and porous morphology. Like other properties, enhanced molecular diffusion is one of the prime features of hierarchical structures, decreasing the bulk to surface diffusion length thus facilitating charge separation.

4. Hierarchical Nanostructured Photocatalysts for CO_2 Reduction

In recent years hierarchical materials designed with either multiple components or intrinsic geometric complexity have drawn great interest for photocatalytic applications. These nanostructures can be categorized based on their structures ranging from one-dimensional to multi-dimensional. It is widely known that the activity of the photocatalysts is dependent upon the interrelated factors of morphology, crystalline size, defects and other surface properties [90]. In the following section, we review the synthesis of hierarchical nanostructures with respect to special morphologies targeted for promoting CO_2 photoreduction.

4.1. Hierarchical Nanostructures with Leaf-Like Morphology

Zhang et al. designed a stable and effective, 3D hierarchical Ru–polypyridine incorporated metal organic framework (MOF) with flower-like morphology for visible-light driven CO_2 photoreduction [91]. In their study, the monodispersed, surfactant less Ru-MOF were synthesized by a simple solvothermal method with controlled morphology tuned with sub-millimeter scale fakes to micro-scale nanoflowers as shown in Figure 2. As per scanning electron microscope (SEM) and transmission electron microscope (TEM) investigations (Figure 2a–f), the as-prepared nanoflowers have diameters in the range of 10–20 μm. While at higher magnification it can be clearly observed that, proper nanoflower morphology constructed with various petals was obtained. Furthermore, these nanoflowers were utilized for CO_2 photoreduction in the liquid phase, along with triethanolamine as a sacrificial agent in 100 mL Schlenk tube under a 500 W Xe lamp irradiation. These Ru-MOF nanoflowers were utilized for heterogeneous photocatalytic CO_2 reduction which produced 24.7 μmol g^{-1} of formate anion ($HCOO^-$) in 8 h irradiation time with quantum yield of 0.67%. The production of $HCOO^-$ was 1.5-fold higher than those of controlled samples such as bulk crystals and micro-fakes. The enhanced activity was attributed to (i) large surface area (surface to volume ratio), (ii) better CO_2 adsorption, and (iii) activation by self-assembled nanoflowers. This study significantly provides some new ideas for fabrication of highly efficient metal organic framework-based photocatalysts for CO_2 reduction. In another example, Dai et al., designed a simple, efficient Bi_2MoO_6 hierarchical nanostructure with three-dimensional (3D) flower like morphology via a hydrothermal synthesis approach. Here, polyvinylpyrrolidone (PVP) was used as a crystal growth modifier [92]. It is believed that polymer molecules adsorb on nanoflakes and act as a crystal phase inhibitor in the system; therefore, PVP plays a crucial role in

fabrication of proper flower-like morphology. Furthermore, the resulting hierarchical nanoflowers were successfully utilized for visible-light-driven CO_2 photoreduction for generation of methanol and ethanol with yield of 24.8 and 18.8 μmol g^{-1} respectively. Here also, the high CO_2 photoreduction activity was ascribed to the high surface area of Bi_2MoO_6. In another study, stable CeO_2/Bi_2MoO_6 heterostructures with flower morphology were prepared via a simple solvothermal route with different weight ratios of CeO_2 to Bi_2MoO_6 [93]. The nitrogen adsorption-desorption technique was used to determine structural properties along with their texture and the results revealed a characteristic mesoporous isotherm. Furthermore, CO_2 photoreduction tests were carried out in water, saturated with CO_2, in presence of visible light (≥420 nm) which resulted in equal amount of methanol and ethanol (58.4 μmol $gcat^{-1}$) as main products for CeO_2/Bi_2MoO_6 (5:100 w/w ratio) sample. The product yield was 1.9 and 4.1 folds higher as compared to that of pure Bi_2MoO_6 and pure CeO_2 respectively. The improved photocatalytic activity of as-obtained heterostructure was referred to high charge carrier separation efficiency of hierarchical nanostructure which was well supported by transient photocurrent responses under visible light irradiation. Furthermore, apart from flower like morphology, Zhou et al. designed the leaf like bio-templated 3D hierarchical perovskite titanates system for CO_2 photoreduction to hydrocarbons fuels, CO and CH_4 [94]. The natural leaf itself contains various components for photosynthesis which efficiently utilize solar light to produce carbohydrates. In this study, perovskite titanates ($ATiO_3$, A= Sr, Ca, and Pb) were designed by preserving the fine morphological details of leaves. In the typical synthesis, green leaves of cherry blossoms were washed and immersed in HCl (5%) solution to get rid of various ions and washed several times with water and ethanol. These leaves were immersed in precursor solutions for 8 h and again washed with ethanol 4 times and dried for one day at 100 °C followed by sintering at 600 °C for 10 h. Here, three types of artificial photocatalysts were synthesized such as $SrTiO_3$ (STO), $CaTiO_3$ (CTO) and $PbTiO_3$ (PTO) respectively by changing the precursors. Furthermore, the loading of co-catalysts (such as Pt, Au, Ag and Cu), RuO_2 and NiO_x was also carried out for comparing CO_2 photoreduction activity. Bare STO and CTO generated CO and CH_4 as main solar fuels in the absence of any sacrificial agents. While, STO and CTO constructed with leaf architecture hierarchical templates revealed enhanced activity of CO and CH_4 to that of bare samples. Such improvement in photocatalytic activity was attributed to escalated gas diffusion and light-harvesting capacity of hierarchical titanates perovskites. Furthermore, loading of co-catalysts such as Au, Ag and Cu on STO-improved CO_2 photoreduction activity, highest with Au (loaded via precipitation), for both CO and CH_4. The study clearly indicates, large variety of plants and biological systems are capable for designing a new class of hybrid photocatalysts that can be applied for diverse energy applications. In another study, CdS hierarchical multi-cavity hollow particles (HMCHPs) possessing fruit (raspberry) like morphology were fabricated for efficient CO_2 photoreduction [95]. Here, CdS HMCHPs were designed by complex nano-architecture with stepwise sequence starting from solution growth, followed by sulfidation, and a cation-exchange approach. As shown in Figure 3a, solid spheres of cobalt glycerate (Co-G) were synthesized by simple mixing of cobalt nitrate and glycerol in isopropanol solution at 130 °C and synthesis of Co-G@ZIF-8 was carried out by growth of a Zn-grounded zeolitic imidazolate framework (i.e., ZIF-8) onto Co-G solid spheres. After that, the Co-G@ZIF-8 composite gained was treated with thioacetamide leading to the formation of CoS_x@ZnS HMCHPs, which later undergoes hydrothermal cation-exchange reaction at 40 °C for 5 h to obtain raspberry morphological-featured CdS HMCHPs (Figure 3a). The SEM images revealed that as-formed CdS HMCHPs clearly shows a raspberry morphology (Figure 3b,c) with a central large cavity containing hollow particles on the shell (Figure 3d). The TEM images (Figure 3e–g), also acknowledged the well-defined HMCHPs were constructed with ultrafine nanoparticles of 0.33 nm crystal lattice spacing (Figure 3g) and selected area (electron) diffraction (SAED) pattern as well further suggest that the as formed CdS HMCHPs are constructed from crystallized nanoparticles. Further CdS HMCHPs were utilized for CO_2 photoreduction along with two references i.e., CdS solid spheres (SSs) and CdS hierarchical structures (HSs). The photoreduction tests were carried out in a typical system containing a mixture of H_2O and acetonitrile with $Co(bpy)_3^{2+}$ (bpy = 2, 2′-bipyridine) as co-catalyst

and triethanolamine (TEOA) as an electron donor, respectively. The CdS HMCHPs exhibited highest CO_2 photoreduction into CO with 1337 μmol h^{-1} g^{-1} yield which was much higher than CdS SSs and HSs samples (Figure 3h). Further selectivity and photocatalytic activity were increased by loading small amount of Au (co-catalyst) with 2.8-fold increased CO generation rate (3758 μmol h^{-1} g^{-1} for 0.25 wt% Au) than that of bare CdS HMCHPs (Figure 3i) with stability of four cycles (Figure 3j). Along with CO generation, a small amount of H_2 was also generated in all the samples. The study of wavelength-dependent yield with appropriate long-pass cutoff filters (such as 400, 420, 455, and 495 nm) clearly revealed that CO_2 photoreduction is encouraged by photoexcitation of Au(25)@CdS HMCHPs and maximum evolution with respect to 400 nm cutoff filter (Figure 3k). The overall high yield of CO was credited to high specific surface area of hollow structures which efficiently promotes large amount of CO_2 adsorption and light-scattering effect. Herein, Au acts as charge trap which restricts the recombination of electrons and holes and effectively promotes charge separation for better photocatalytic activity. Therefore, these examples of hierarchical nanostructures containing flower-, leaf- and fruit-like morphologies proved as potential materials for CO_2 photoreduction.

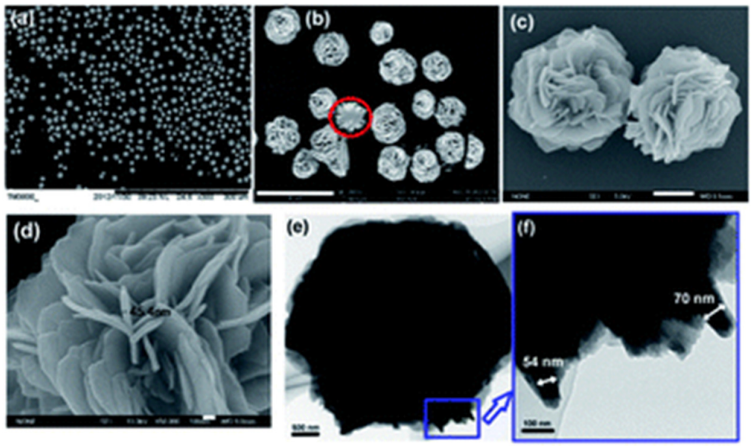

Figure 2. (**a**–**d**) Scanning electron microscope (SEM) and (**e**,**f**) transmission electron microscope (TEM) images of Ru-metal-organic framework (MOF) nanoflowers at different magnifications, reprinted with permission from [91].

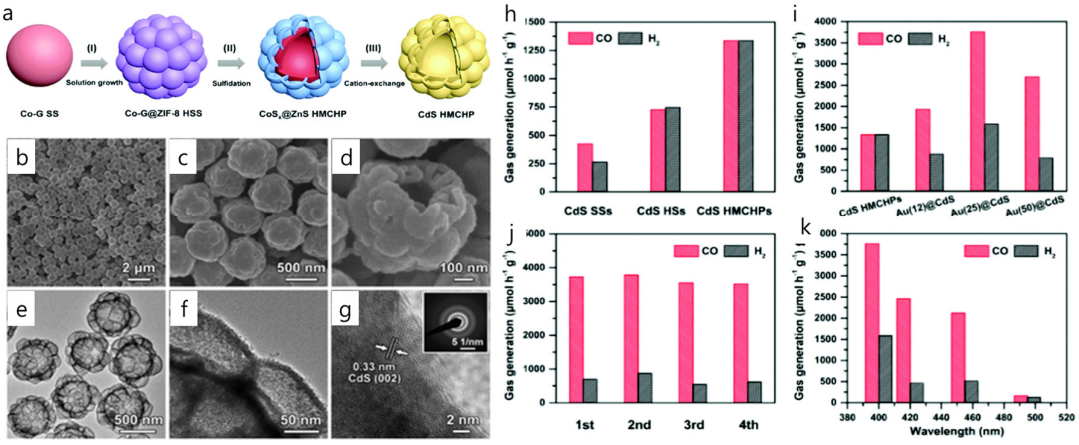

Figure 3. (**a**) Stepwise formation process of CdS hierarchical multi-cavity hollow particles (HMCHPs), (**b**–**d**) FESEM, (**e**–**g**) TEM and high-resolution transmission electron microscope (HRTEM) images, (**g**) SAED pattern of CdS HMCHPs, (**h**) The CO_2 photocatalytic activity of various samples, (**i**) Photocatalytic activity of CdS HMCHPs with different Au loadings, (**j**) Evolution of CO and H_2 using Au(25)@CdS sample and (**k**) The wavelength-dependent yields for Au(25)@CdS sample, reprinted with permission from [95].

4.2. Hierarchical Nanosphere Morphologies

Among the diverse structures, another way to attain the desirable photocatalytic behavior is the fabrication of spherical hierarchical nanostructures due to their immense features such as high porosity, high surface area, low bulk density and reflection of light in the interior cavities [96]. In this regard, Fang et al. reported mesosphere of TiO_2 hierarchical nanostructure for photocatalytic CO_2 reduction [97]. The synthesis was carried out by employing the sol-gel technique. In detail, the desired amount of C_2H_5OH was mixed with deionized water (H_2O) followed by the addition of concentrated HCl and titanium isopropoxide. After that, aqueous solution of chitosan glacial acetic acid along with NH_4OH were added and calcinated at 450 °C for 3 h to get resulting TiO_2 spheres. Morphological features from the digital (Figure 4a) as well as SEM images (Figure 4b) reveal that as-formed dense TiO_2 particles have spherical morphology. At high magnification, the surface was observed to be tightly packed with small particles comprising mesoporous morphology. Furthermore, CO_2 photoreduction investigation was carried out using a batch reactor under Hg UV lamp (40 W, 254 nm) irradiation for 24 h. The results showed that, as-prepared spherical TiO_2 yielded 0.94, 2.32 and 2.03 μmol g^{-1} h^{-1} of CH_4, CO, and H_2, respectively which is higher than bare P25. The Pt-loaded TiO_2 spheres with various Pt contents were synthesized. The results clearly revealed that, with 0.6% loading of Pt there is 20-times increment in CH_4 generation than pure P25. The improved catalytic activity and selectivity (CH_4) of TiO_2 spheres over bare P25 was attributed to the enhanced multiple scattering, mesoporous volume, hierarchical porosity and large hollow channels that facilitates the fast mass transport within the special structure. In another similar study, porous TiO_2 microspheres were developed by Di et al. employing a microwave assisted solvothermal method in combination with heat treatment in air [98].

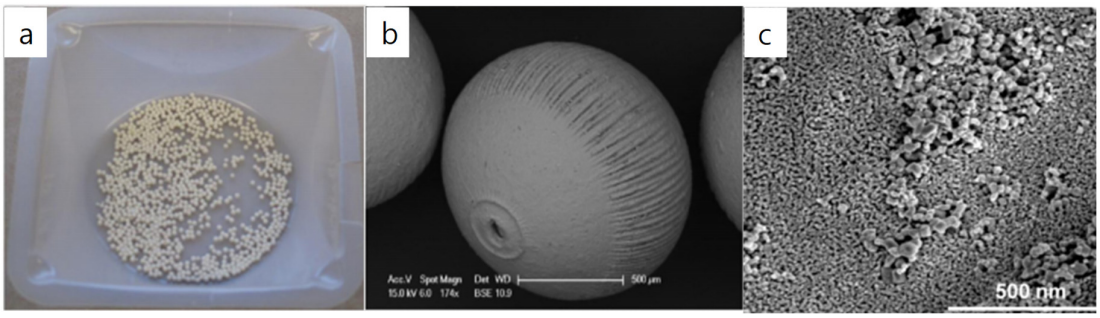

Figure 4. (**a**) The digital image and (**b**,**c**) SEM images of as-obtained TiO_2 spheres, reprinted with permission from [97].

The morphological study reveals that as formed TiO_2 hierarchical microspheres were well arranged into nanosheets with porous features. The high surface area of the TiO_2 hierarchical nanostructure, i.e., 142 m^2 g^{-1} was confirmed by N_2 adsorption-desorption along with enhanced pore size distribution as compared to anatase TiO_2. Similarly, CO_2 uptake capacity of TiO_2 hierarchical photocatalyst was 0.42 μmol g^{-1} which was almost double that of anatase TiO_2, 0.25 μmol g^{-1}. These collective features such as high specific surface area, large pore volume and enhanced CO_2 uptake ability of spherical-shaped TiO_2 hierarchical nanostructures play an important role in boosting CO_2 photoreduction activity. A CO_2 photoreduction test was carried out in a batch reactor employing Hg UV lamp (40 W) as a light source for 1 h illumination time. The results showed that, CH_4 and CH_3OH were obtained as main products with yields of 0.23 and 0.08 μmol respectively which were much higher than pure P25 and anatase TiO_2. The band structure of TiO_2 hierarchical nanostructure was analyzed using the Mott–Schottky measurement and the result showed that the band gap potential obtained is more negative than the redox potential of photocatalytic reactions which endows stronger reduction ability. Therefore, the improved photocatalytic activity was attributed to ultrathin microspheres with large specific surface area which eventually creates many active sites for CO_2 adsorption and further helps to improve the overall CO_2 photoreduction yield. In 2016, Pan et al. reported the self-assembled

hollow spheres of $LaPO_4$ photocatalysts for enhanced CO_2 photoreduction into hydrocarbon fuels [86]. In their study, citric acid was utilized as a structure-directing agent for the fabrication of $LaPO_4$ hollow spheres via a facile solution route and growth mechanism of as prepared hierarchical structures and was studied in a solution-phase. Typical synthesis of $LaPO_4$ spheres began with the formation of a lanthanum metal citrate complex by mixing lanthanum nitrate and the desired amount of aqueous solution of citric acid followed by metal complex dissolution in H_3PO_4 aqueous solution to form the desired hierarchical structure. The uniformly distributed monodispersed microsphere morphology was confirmed from low magnified SEM images (Figure 5a). While at higher magnifications, spines like $LaPO_4$ 3D microspheres were observed with diameters of 600-800 nm. The results were well supported by TEM images where it can be clearly seen that individual microspheres were densely arranged by nanorods with diameters of 10-20 nm. The citric acid ratio in synthesis of $LaPO_4$ was varied from 0, 10, 100 and 500 mg for comparing the results with respect to their photocatalytic activity. Here, citric acid plays a crucial role in the formation of the hierarchical structure (Figure 6). It can be clearly seen that, in absence of citric acid, the isolated nanorods (Figure 6a) were obtained while with introduction of 10 mg citric acid, the 3D microspheres with diameter of 1.28 μm appeared (Figure 6b). In addition to this, at 100 mg citric acid (Figure 6c), the morphology remained unchanged with only modification in the diameter (600–800 nm).

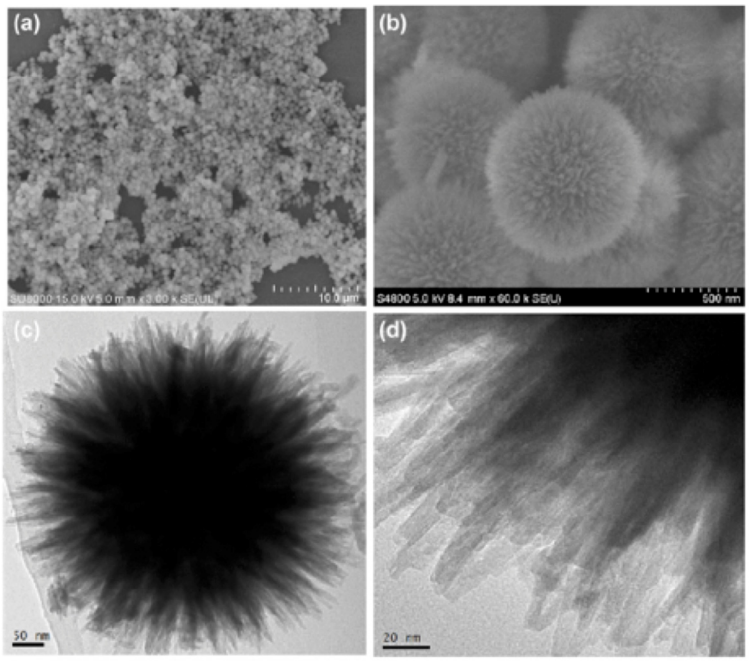

Figure 5. The SEM images (**a**,**b**) and TEM image (**c**,**d**) images of $LaPO_4$-Citric acid-100 sample, reprinted with permission from [86].

At 500 mg concentration, half-baked microspheres with 300-400 nm diameter were formed as shown in Figure 6d. Therefore, in such a solution phase reaction, coordination of H_3PO_4 and citric acid is very important to obtain the desired spherical morphology. The CO_2 photoreduction results revealed that CH_4 (10.5 μmol) was obtained as a main product along with generation of small amount of H_2 (6.3 μmol) after 5 h irradiation. The as-synthesized 3D $LaPO_4$ hierarchical mesosphere structures exhibited a 6.2-fold increased photocatalytic activity compared with 1D $LaPO_4$ nanorods. The outcome of better catalytic activity was mainly credited to: the (i) hollow structure, (ii) enhanced light-harvesting ability, and (iii) remarkable charge-carrier separation capability of spheres.

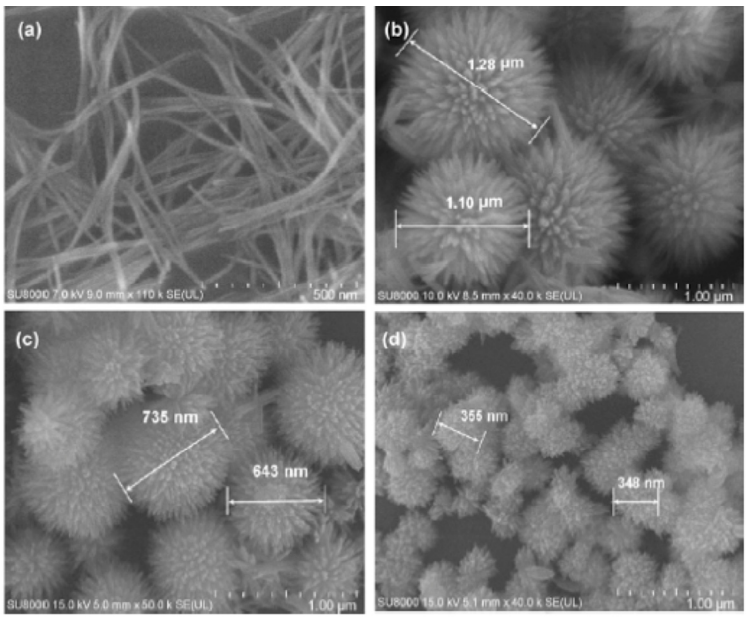

Figure 6. The SEM images of $LaPO_4$ with change in citric acid amount (**a**) 0 mg, (**b**) 10 mg, (**c**) 100 mg and (**d**) 500 mg, reprinted with permission from [86].

In 2015, Ho's group reported Z-scheme CdS-WO_3 photocatalyst for CO_2 photoreduction into CH_4 in the presence of visible light [99]. Here, WO_3 hierarchical hollow spheres were first synthesized and CdS nanoparticles were grown on hollow spheres to obtain Z-scheme heterostructure. The maximum photocatalytic activity for CO_2 reduction into CH_4, 1.02 µmol h^{-1} g^{-1} was reported for the optimized CdS–WO_3 sample (with 5 mol% CdS content) which was 100 and 10 times higher than that of bare WO_3 and CdS, respectively. The BET specific surface area, calculated by employing N_2 adsorption-desorption isotherms, confirmed the mesoporosity with the range of 2-50 nm while pores shape was confirmed by using pore (0.8-1) structure study. In another study, Lin et al. developed hybrid complex/semiconductor (spherical shaped) heterophotocatalyst by employing feasible hydrothermal method [100]. In this study, spherical TiO_2 hybridization with a cobalt complex i.e., $[Co(bipy)_3]^{2+}$ structure was fabricated. The photocatalytic CO_2 reduction results showed that the photocatalyst possessing spherical morphology has a high surface area which exhibits a superior CO_2 photoreduction performance compared to that of bulk TiO_2. The morphological features obtained from SEM (Figure 7a) and TEM (Figure 7b,c) images clearly indicate that, the as prepared TiO_2 nanostructures were spherical in shape, and well-arranged into nanosheets. Furthermore, the N_2 adsorption-desorption isotherm study revealed that as-prepared TiO_2 having a mesoporous structure represented a type-IV isotherm with a hysteresis loop of type H_3 as shown in Figure 7d. Due to such porous morphology, the BET surface area was coming out as 136 m^2 g^{-1}, a much higher than bulk TiO_2 (14 m^2 g^{-1}). The H_2 and CO were obtained as the main products with yield of 6.6 and 16.8 µmol respectively using TiO_2 containing $Co(bipy)_3^{2+}$ hybrid system. Therefore, a hollow spherical TiO_2 hierarchical structure plays an important role in CO_2 photoreduction which allows efficient charge transfer to cobalt complex onto the surface and acts as a photon trap and eventually enhances the light absorption. Henceforth, all these examples proved that, such spherical morphology acquired hierarchical nanostructures can be considered as an efficient and potential CO_2 photoreduction photocatalysts in future prospective.

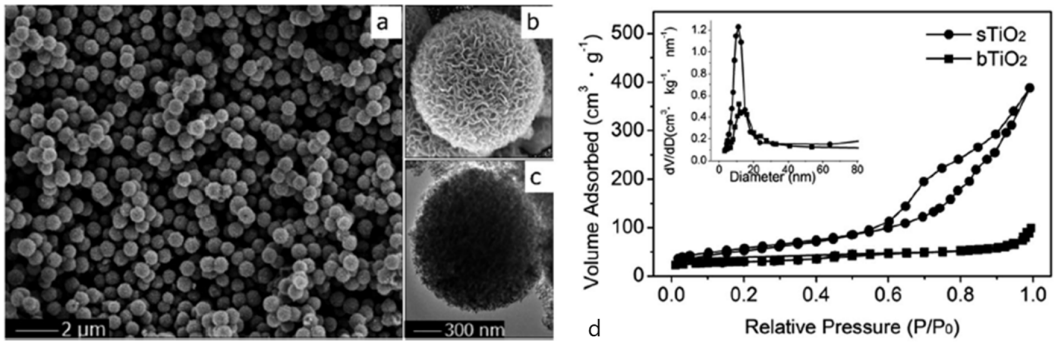

Figure 7. The (**a**) SEM, (**b**,**c**) TEM images and (**d**) N_2 adsorption-desorption isotherm of spherical ($sTiO_2$) and bulk ($bTiO_2$) samples (inset pore size distribution), reprinted with permission from [100].

4.3. Fiber-Like Hierarchical Materials

The properly designed 1D structures such as fibers/nanofibers have also been utilized for solar light harvesting due to their efficient photochemical properties. While 1D nanomaterials were considered as one of the ideal material to fabricate hierarchical heterostructures as a function of high surface area along with enhanced charge transfer ability [101,102]. Numerous synthesis approaches have been developed to acquire ideal nanofiber morphology with controlled reaction systems. For instance, Renones et al. in 2016 fabricated nanofibers of TiO_2 by combining electrospinning and sol–gel techniques and studied the photocatalytic behavior [103]. The TiO_2 nanofibers were synthesized by the electrospinning method while for comparison with respect to photocatalytic performance, TiO_2 nanoparticles were prepared by employing sol-gel technique. Morphological features using SEM (Figure 8a,b) and TEM (Figure 8c,d) clearly depicted the formation of nanofibers. The pore size of the as-prepared hierarchical fibers was reported to be 20 nm which was much higher than normal TiO_2 (4.7 nm). Further, these 1D hierarchical nanofibers were utilized for CO_2 photoreduction in gas phase using continuous flow reactor under UV light (λ_{max} = 365 nm) irradiation. After 20 h irradiation CO, CH_4, CH_3OH and H_2 were obtained as main products with yield of 23.91, 26.88, 5.04 and 398.84 µmol g^{-1} catalyst, respectively. The yield and selectivity of the hierarchical nanofibers was much higher than that of regular TiO_2 nanoparticles with 0.030% apparent quantum yield (AQY).

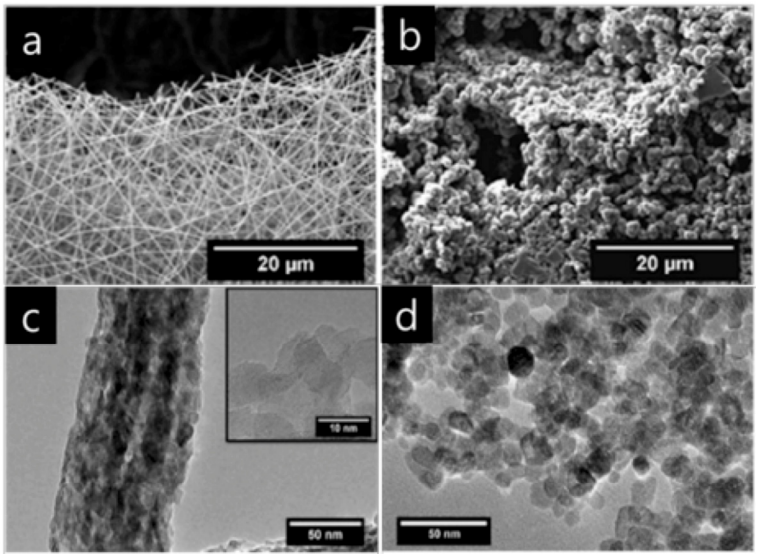

Figure 8. The SEM images of (**a**) TiO_2 fibers, (**b**) TiO_2 prepared using sol-gel method and TEM images of (**c**) TiO_2 fibers, and (**d**) TiO_2 prepared using sol-gel method, reprinted with permission from [103].

In another study, Meng et al. synthesized a hierarchical $TiO_2/Ni(OH)_2$ composite by loading $Ni(OH)_2$ on TiO_2 fibers [26]. In typical synthesis (Figure 9a), TiO_2 nanofibers were first prepared using the electrospinning technique followed by calcination and precipitation to get the desired product i.e., $TiO_2/Ni(OH)_2$ composite with varied weight ratios of $Ni(OH)_2$ (i.e., 0.5, 1, 1.5, 2 or 15%). Field emission SEM (FESEM) (Figure 9b), and TEM images (Figure 9d,e) revealed the existence of nanofiber morphology. Here, TiO_2 nanofibers acted as backbone for the growth of $Ni(OH)_2$ as shown in Figure 9b. Further, CO_2 uptake ability of as-prepared samples was estimated by employing CO_2 adsorption isotherms. The results demonstrated that, sample of $TiO_2/Ni(OH)_2$ containing 15% weight ratio of $Ni(OH)_2$ exhibited almost two-fold higher CO_2 adsorption capability than bare TiO_2 nanofibers.

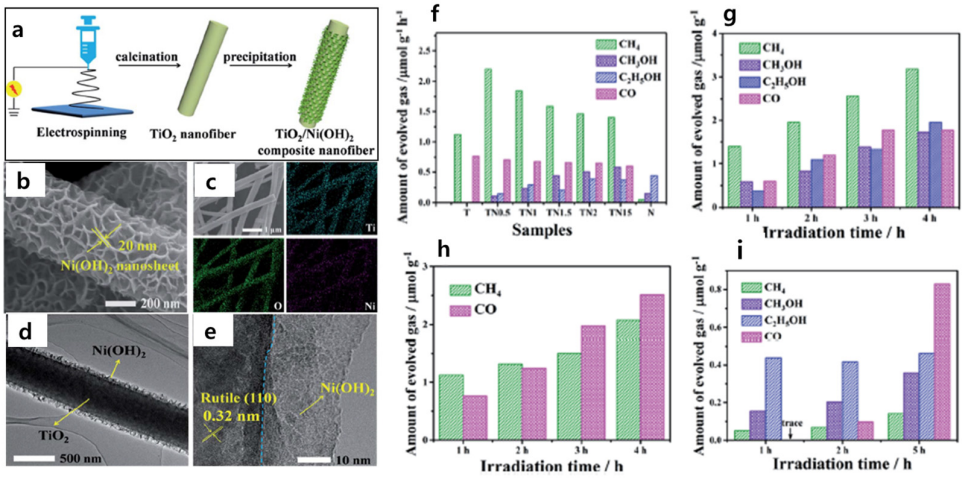

Figure 9. (**a**) Synthesis illustration of hierarchical $TiO_2/Ni(OH)_2$ hybrid composite, (**b**) SEM, (**c**) energy-dispersive X-ray spectroscopy (EDX) mapping, (**d**,**e**) TEM images of $TiO_2/Ni(OH)_2$ with 15 wt% $Ni(OH)_2$ loading and (**f**–**i**) the photocatalytic CO_2 reduction behavior of various samples, reprinted with permission from [26].

Therefore, $Ni(OH)_2$ acts as an CO_2 adsorbent which further plays an important role in enhancing the CO_2 photoreduction activity. Indeed, solar light illumination (300 W Xe lamp) of as-prepared TiO_2 fibers showed that CH_4 and CO were the main products for all the samples (Figure 9f). Also, after increasing $Ni(OH)_2$ content of 0.5 wt%, the notable amount of CH_3OH and C_2H_5OH also achieved. Maximum yields for CH_3OH, 0.58 μmol h^{-1} g^{-1} and C_2H_5OH, 0.37 μmol h^{-1} g^{-1} were appeared with 15 wt% loading. However, time-coursed photocatalytic fuel production over different samples was also carried out as depicted in Figure 9g–i and results proved that photocatalytic CO_2 conversion to various fuels can be greatly enhanced by using such hybridized hierarchical nanofibers. In addition to such hybrid hierarchical nanofibers, $CuInS_2$ sensitized TiO_2 hybrid nanofibers were successfully synthesized by Xu et al. by employing a Z-scheme heterojunction [104]. Such nanofibers were synthesized using a simple electrospinning setup and further $CuInS_2$ were grown via hydrothermal synthesis approach with varied concentration of precursor. The resulting $CuInS_2$ sensitized TiO_2 hybrid nanofibers outperformed for CO_2 photoreduction to obtain CH_4 and CH_3OH as the main products under a 350 W solar Xe lamp irradiation using a homemade Pyrex reactor. After 1 h irradiation, the hybrid composite with 2.5 wt% $CuInS_2$ loading generated CH_4 and CH_3OH as the main products through production of 2.5 and 0.85 μmol h^{-1} g^{-1}, respectively. Enhanced CO_2 photoreduction performance was attributed to the extended light absorption, increased surface area of hierarchical nanostructure and generation of Z-scheme heterojunction. Hierarchical, 1D/2D, TiO_2/MoS_2 hybrid nanostructures containing TiO_2 fibers were constructed via a hydrothermal transformation method by Xu et al. [105]. The typical synthesis involved, in situ growing of MoS_2 (2D) nanosheets on the nanofibers of TiO_2 (1D) to obtain 1D/2D hybrid hierarchical nanostructure which enhanced optical absorption along with increased CO_2 adsorption compared to those of pristine TiO_2 and MoS_2. The formation of TiO_2

nanofibers was confirmed by SEM images with a diameter of about 200 nm (Figure 10a). While after insertion of MoS_2 on the surface of TiO_2 nanofibers, the surface of fibers became larger and denser upon increasing the concentration of MoS_2 from 10 wt% to 25 wt% (Figure 10b,c). The microstructures in 10% MoS_2/TiO_2 were clearly observed in TEM and HRTEM images comprising lattice d spacing of 0.352, 0.325 and 0.62 nm corresponding to anatase (101) TiO_2, rutile (110) TiO_2 and MoS_2 facets respectively (Figure 10d,e). The EDX mapping images of 10% MoS_2/TiO_2 confirmed the presence of Ti, O, Mo and S elementals which represent the successful hybridization of TiO_2 and MoS_2 hierarchical composite (Figure 10f). The N_2 adsorption-desorption isotherms of pristine TiO_2, pristine MoS_2 and hybrid 1D/2D nanostructures were measured and the results revealed that all samples exhibit a type-IV isotherm and type-H_2 hysteresis loop with a 0.45–0.9 P/P_0 range. The results clearly illustrate the mesoporous nature of TiO_2 nanofibers which could be due to MoS_2 nanosheets. Hybrid MoS_2/TiO_2 hierarchical photocatalyst with 10 wt% MoS_2 loading exhibited enhanced performance compared to pristine TiO_2 and MoS_2. The photocatalytic CO_2 reduction results showed CH_4 and CH_3OH were the main products yielding 2.86 and 2.55 μmol g^{-1} h^{-1}, respectively, along with trace amounts of CO formation. Such improved catalytic activity of the fiber nanostructure was attributed to high surface area, improved light absorption after hybridization, increased CO_2 adsorption capacity and the presence of MoS_2 nanosheets which improved charge separation. Referring to the aforementioned discussion it can be established that the photocatalysts with fiber-like hierarchical hybrid composites can be employed for sustainable and efficient CO_2 photoreduction to solar fuel generation.

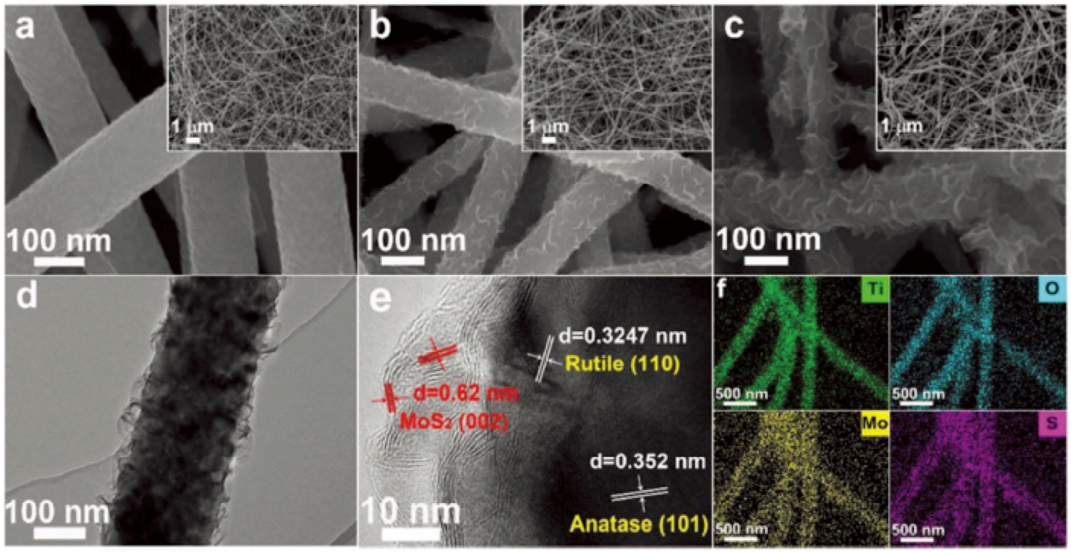

Figure 10. SEM images of (**a**) pristine TiO_2 fibers, (**b**) 10% MoS_2/TiO_2, (**c**) 25% MoS_2/TiO_2; (insets: corresponding low-magnification SEM images), (**d**) TEM, (**e**) HRTEM images and (**f**) EDX element mappings for 10% MoS_2/TiO_2, reprinted with permission from [105].

4.4. Hierarchical Tube/Rod Morphologies

In general, an ideal photocatalyst should possess better photochemical properties, enhanced surface activity therefore optimization and fabrication of photocatalysts with the desired size and shape is prime objective of photocatalysis in CO_2 photoreduction systems. However, to maximize the performance of photocatalysts, the design with proper nanostructure is also indispensable. The 1D nanotubes with hollow and porous morphology also proved to be effective for CO_2 photoreduction. These hierarchical nanotubes can facilitate separation and migration of photogenerated charges and enhance the adsorption of the CO_2 molecule which offers active sites for redox reaction on the surface of the catalyst [106].

Fu et al. fabricated O-doped graphitic carbon nitride (O-C_3N_4) hierarchical nanotubes by employing thermal oxidation exfoliation and curling-condensation of bulk g-C_3N_4 for CO_2

reduction [87]. Bulk g-C_3N_4 was prepared by using melamine as starting material and employing thermal polycondensation followed by exfoliation to get g-C_3N_4 nanosheets. After condensation of g-C_3N_4 nanosheets the one dimensional (1D), g-C_3N_4 nanotubes were obtained. Meanwhile, O-doping was carried out by substituting C or N atoms during high-temperature oxidation process in airflow to get desired photocatalysts (OCN-tubes).

The uniform porous network structure was well observed from SEM images without bulk agglomerate while in case of bulk g-C_3N_4, the agglomerated morphology was noticed. While distinct TEM images confirmed the 1D tubular nanostructure of typical multi-walled carbon nanotubes (MWCNTs). Thus, such hierarchical structures due to their distinct features such as: (i) high specific surface area, (ii) multiple scattering in between channels, (iii) exposed active edges, (iv) excellent CO_2 uptake ability, and (v) enhanced molecular diffusion kinetics, can be designated as promising CO_2 reduction photocatalysts. As a result, hierarchical OCN-tube displayed CH_3OH formation of 0.88 μmolg^{-1} h^{-1}, which exhibited five-fold higher photocatalytic performance compared to that of bulk g-C_3N_4 (0.17 μmol g^{-1} h^{-1}). These results are coherent to N_2 adsorption–desorption isotherms with corresponding pore size distribution curves (Figure 11a). The meso and macroporous nature of 1D nanotubes was detected with 0.128 cm^3 g^{-1} pore volume higher than that of bulk g-C_3N_4 (0.037 cm^3 g^{-1}). The enhanced photo absorption of the OCN-tube in the visible region was confirmed by ultraviolet–visible (UV–Vis) diffusion reflectance spectra (DRS) as shown in Figure 11b. The increased absorption was attributed to the multiple reflection of light inside the hierarchical multi-walled nanotubes. Considering the tubular hierarchical architectures with their own special properties, Wang et al. in 2017 fabricated novel, self-templated, In_2S_3-$CdIn_2S_4$ heterostructures for efficient CO_2 reduction accounting for solar fuel production [105]. In short, MOF (MIL-68) hexagonal prisms were first prepared and hierarchical In_2S_3 nanotubes were prepared by a liquid phase sulfidation approach and finally hierarchical In_2S_3-$CdIn_2S_4$ were collected by cation exchange reaction. The FESEM and TEM images revealed 1D tubular morphology with ultrathin sheet-shaped subunits as shown in Figure 12a–f. After evaluation for CO_2 photoreduction, it was observed that optimized tubular In_2S_3-$CdIn_2S_4$ sample generated a noticeable amount of CO (825 μmol h^{-1} g^{-1}) in addition to a small amount of H_2 (Figure 12g). While the efficiency of CO was 12-fold higher than pristine In_2S_3 along with an enhanced selectivity and stability. Such high performance was attributed to unique tubular morphology displaying reduced diffusion length, large surface area, enhanced CO_2 adsorption ability and compositional features of the photocatalyst.

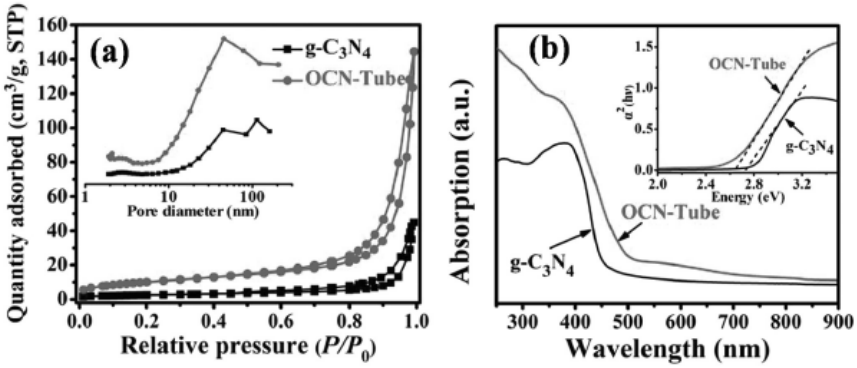

Figure 11. (**a**) N_2 adsorption–desorption isotherms along with corresponding pore size distribution curves and (**b**) ultraviolet–visible (UV–Vis) diffusion reflectance spectra (DRS) of bulk and OCN-tube, reprinted with permission from [87].

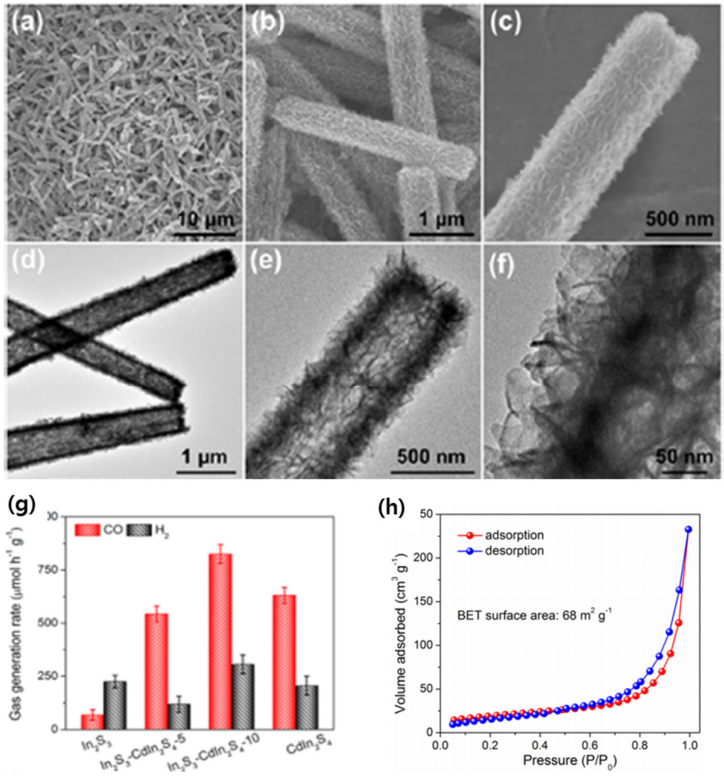

Figure 12. (**a**–**c**) Field emission SEM (FESEM) images, (**d**–**f**) TEM images, (**g**) CO_2 photoreduction performance and (**h**) N_2 adsorption isotherms of In_2S_3-$CdIn_2S_4$ hierarchical nanotubes (with optimized sample), reprinted with permission from [106].

The CO_2 photoreduction results were further supported by N_2 adsorption isotherms (Figure 12h) of a hierarchical nanotube possessing a high BET surface area (68 m^2 g^{-1}) and exhibiting a high CO_2 uptake of ca. 25 cm^3 g^{-1} at 760 mmHg. The as-prepared photocatalyst exhibited selectivity for 6 cycles without any deactivation which proves its superiority as compared to other traditional photocatalysts. In addition to this work, Wang et al. in 2018, designed a sandwich-like $ZnIn_2S_4$–In_2O_3 hierarchical heterostructures acquired tubular morphology owing high stability and superior CO_2 photoreduction performance into deoxygenation to form CO as the main product [107]. In this study, $ZnIn_2S_4$ nanosheets were well assembled on the inside as well as on the outer surfaces of In_2O_3 to form a tubular sandwich-like $ZnIn_2S_4$–In_2O_3 double heterojunction. SEM images (Figure 13a–c) demonstrated uniform coverage of $ZnIn_2S_4$ on the surface of In_2O_3 which had a well-maintained 1D tubular morphology with open ends. At higher magnification (Figure 13c), $ZnIn_2S_4$ layers composed of nanosheets were grown on a In_2O_3 microtubular surface to form sandwich like heterostructure. Afterwards, such highly porous, hollow interiored nanotubes were utilized for CO_2 photoreduction and results exhibited the formation of CO as a main product in addition with noticeable amount of H_2 (Figure 13d,e). Here, the mixture of H_2O/acetonitrile with $Co(bpy)_3^{2+}$ (bpy = 2, 2′-bipyridine) was used as co-catalyst and triethanolamine (TEOA) was used as an electron donor to conduct the CO_2 photoreduction test. The optimized sample produced CO with yield of 3075 μmol h^{-1} g^{-1} which was recorded much higher than bare $ZnIn_2S_4$ particles (875 μmol h^{-1} g^{-1}) and $ZnIn_2S_4$ NSs (1275 μmol h^{-1} g^{-1}) as shown in Figure 13d. The high activity was due to the large specific surface area (128 m^2 g^{-1}) of $ZnIn_2S_4$-In_2O_3 exhibiting porous features possessing the maximum CO_2 uptake ability of ca. 20 cm^3 g^{-1} at 0 °C. The transient photocurrent spectra also evidenced that as-prepared hierarchical structure exhibited enhanced photocurrent which was due to transfer of photogenerated charges in heterojunction system (Figure 13f). Therefore, such types of efficient materials possessing special morphology may inspire the development of artificial photocatalytic system for real and large-scale application.

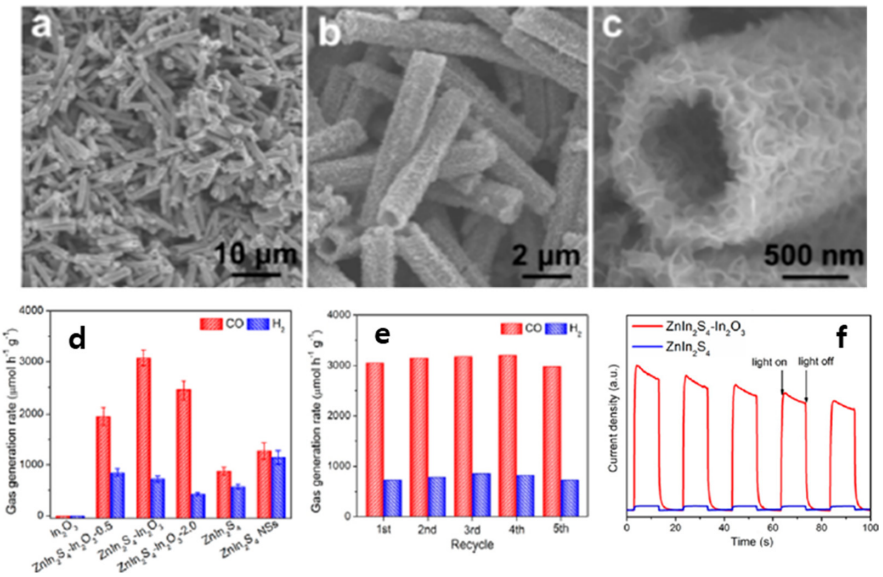

Figure 13. (**a**–**c**) FESEM images of $ZnIn_2S_4$–In_2O_3, (**d**) Photocatalytic CO_2 reduction activities of different samples, (**e**) Stability test and (**f**) Transient photocurrent spectra of hierarchical $ZnIn_2S_4$–In_2O_3 and $ZnIn_2S_4$ samples, reprinted with permission from [107].

Xiao et al. constructed hierarchical assemblies of Bi_2WO_6 acquiring a hollow and rod-shaped appearance [85]. To fabricate hierarchical Bi_2WO_6 structures, a solid Bi precursor was prepared and employed as a template to obtain a hollow morphology of Bi_2WO_6 because of the Kirkendall effect. The as-obtained hierarchical Bi_2WO_6 structures were composed of numerous nanosheets on the surface of hollow micro-rods as shown in Figure 14a. When the surface was practically broken, it was observed that nanosheets are uniformly decorated around the particles with a hollow interior of microrods (Figure 14b). In addition, the TEM image (Figure 14c) of Bi_2WO_6 hierarchical rods further confirmed its hollow feature with average shell thickness of about 300 nm. This study reveals that CO_2 photoreduction activity of as-obtained Bi_2WO_6 hierarchical rods is much higher as compared to bulk Bi_2WO_6. The CO_2 reduction was carried out under Xe lamp irradiation and 2.6 μmol g^{-1} h^{-1} CH_4 yield was achieved which was 8-fold higher than bulk Bi_2WO_6 along with a high recycling stability. The band gap investigation was carried out by using UV-vis DRS and a Mott–Schottky plot and outcomes indicated that the band gap of hierarchical Bi_2WO_6 (2.92 eV) is larger than bulk Bi_2WO_6. While the conduction band (CB) edge of the hierarchical Bi_2WO_6 rod was lower than redox potentials of CO_2/CH_4 (−0.24 V vs. reversible hydrogen electrode (RHE)), making it thermodynamically feasible for CO_2 reduction to CH_4. The N_2 adsorption-desorption isotherm was recorded to understand the nature of the material and results confirmed that as-prepared material possesses meso-/macro-porous morphology with district hysteresis loop in between 0.5-1.0 P/P_0. Henceforth, such hierarchical tubes/rods are considered as potential photocatalysts for advanced practical application in CO_2 photoreduction to various solar fuels.

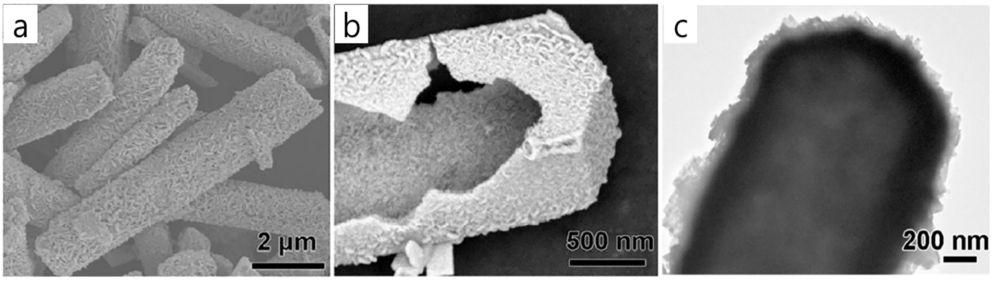

Figure 14. (**a**,**b**) SEM and (**c**) TEM images of hierarchical Bi_2WO_6 nanorods, reprinted with permission from [85].

4.5. Sheet-Like Hierarchical Materials

In addition to photocatalysts morphologies, 2D nanosheets hierarchical structures have also garnered enormous attention in CO_2 photoreduction process field. Hierarchical structured ZnV_2O_6 nanosheets, synthesized by one-step solvothermal method, when used for CO_2 photoreduction, showed extraordinary catalytic activity [108]. As-prepared ZnV_2O_6 nanosheets possess high surface area (BET) of 11.57 m^2 g^{-1} and smaller pore diameter of 17.3 nm due to its hierarchical structure which played important role in minimizing mass transfer limitations and eventually increases the overall catalytic performance. In UV-Vis spectra, the ZnV_2O_6 nanosheets displayed absorption in the visible region with band gap of 2.02 eV. The SEM images revealed surface morphology of a hierarchical microstructure composed of uniform-sized nanosheets while the SAED pattern showed a ring of polycrystalline due to good crystalline nature of ZnV_2O_6. The CO_2 photoreduction performance of as-prepared ZnV_2O_6 nanosheets was measured using a slurry type photoreactor with quartz glass under visible light irradiation (35 W high-intensity discharge (HID) Xe lamp) at room temperature. Employing ZnV_2O_6, the CH_3OH, HCOOH and CH_3COOH were obtained as resulting solar products with a yield of 3253.84, 2886.9 and 530.1 μmol g^{-1} respectively. While 48.78% selectivity of ZnV_2O_6 towards CH_3OH was achieved in current photocatalytic system which was attributed to its hierarchical structure possessing enhanced charge separation. Apart from the role of the main catalyst, 2D nanosheeets were also used as co-catalysts in photocatalytic processes. Jung et al. designed a ternary hierarchical hybrid structure containing mesoporous TiO_2 on graphene containing few layered 2D MoS_2 sheets via a one pot hydrothermal route [109]. The graphene played an important role to reduce the channel length of 3D structure and shorten the diffusion length for photogenerated carriers. However, 2D MoS_2 sheets were used as co-catalyst as it possesses high robustness and layer-dependent photoactivity. Therefore, in a typical hierarchical structure 2–3 layered MoS_2 were formed simultaneously with TiO_2 and graphene oxide (GO) during a one-pot hydrothermal process. The SEM and TEM images revealed that, 2D rGO sheets were assembled with a microporous nature while TiO_2 particles and MoS_2 sheets were uniformly covered over the graphene surface to form a hierarchical porous structure. The decreased photoluminescence intensity revealed the effective charge transfer of photogenerated carriers and delayed the recombination rate which played an important role in CO_2 photoreduction. The CO_2 reduction results exhibited that, CO was main product with selectivity of 97%. While, CO formation rate in optimized sample of TiO_2-graphene-MoS_2 hierarchical structure was 92.33 μmol g^{-1} h^{-1} which was 14.5-fold higher than the bare TiO_2. The photo-excited electrons generated from TiO_2 and graphene were accommodated on the surface of the MoS_2 where the CO_2 molecules were reduced to form CO as a solar product. Here, combination of microporous 3D graphene along with microporous TiO_2 and 2D-MoS_2 co-catalyst hierarchical nanostructured system helped to enhance the overall CO formation rate. Therefore, such studies highlight the promising ways of fabrication of efficient and high-performance photocatalysts for CO_2 photoreduction.

4.6. Hierarchical Nanoboxes

The prevention of unwanted aggregation and improvement in light absorption can be achieved by highly porous, hollow, three-dimensional (3D) nanoboxed hierarchical structures. For example, Qiu et al. successfully designed CdS/Co_9S_8 hollow cubes containing a cubic (box) structure and employed for photocatalytic water splitting [110]. They observed that hollow cubes exhibited stronger light absorption due to multi-light scattering/reflection inside the cavities of hollow architecture which enhanced overall photocatalytic performance. In this regard, Wang et al. in 2018, constructed complex hierarchical nanoboxes of nitrogen-doped carbon@$NiCo_2O_4$ (NC@$NiCo_2O_4$) for efficient visible light CO_2 reduction [82]. The as-prepared hybrid hierarchical nanoboxes containing hollow features possess both morphological and functional advantages such as enhancement in charge separation and increased CO_2 adsorption on the surface which offers more active sites for photocatalytic reaction. Figure 15a presents stepwise synthetic illustration of complex hierarchical NC@$NiCo_2O_4$ nanobox including, (i) Fe_2O_3@PDA core-shell formation via sol-gel followed by (ii) N-doped carbon formation after

heating in a N_2 atmosphere. Finally, (iii) $NiCo_2O_4$ nanosheets were grown on NC nanoboxes through a hydrothermal approach followed by thermal treatment to obtain NC@$NiCo_2O_4$ double-shelled nanobox hierarchical structure. The FESEM images of nanoboxes revealed its cubic nature (Figure 15b,c) while at higher magnification (single nanobox) it can be observed that, NC@$NiCo_2O_4$ nanobox is enclosed with $NiCo_2O_4$ ultrathin sheets subunits (Figure 15d). The TEM and HRTEM images also acknowledged: (i) hollow nanostructured morphology and (ii) formation of $NiCo_2O_4$ nanosheets with interlayer distance of 0.28 and 0.46 nm corresponding to (220) and (111) crystal planes of $NiCo_2O_4$ (Figure 15e–g). While the SAED pattern gives information about the polycrystalline nature of $NiCo_2O_4$ nanosheets, elemental mapping calculated from EDX spectra revealed the presence of necessary elements (Figure 15h). The obtained nanobox contained a hollow architecture with high specific surface area of 142 m^2 g^{-1}. In addition, the CO_2 adsorption isotherm calculation exhibited higher CO_2 uptake of 60 cm^3 g^{-1} (at 0 °C) which was higher compared to bulk $NiCo_2O_4$ particles. Henceforth, these features of hierarchical nanoboxes actively promote deoxygenation of CO_2 to form the useful solar fuel, CO. The CO_2 photoreduction tests were carried out under visible light irradiation in H_2O/acetonitrile mixture using $[Ru(bpy)_3]Cl_2.6H_2O$ as photosensitizer and triethanolamine (TEOA) as electron donor. As a result, hierarchical NC@$NiCo_2O_4$ nanoboxes exhibited 26.2 μmol h^{-1} of CO which was higher than bulk $NiCo_2O_4$ (Figure 15i). To understand the effects of nanobox morphology, CO_2 photoreduction was carried out under different reaction conditions and the results are illustrated in Figure 15i. In particular, NC@$NiCo_2O_4$ nanoboxes exhibited excellent selectivity (86.6%) towards CO production along with the formation of a small amount of H_2. Additionally, the resulting CO_2 photoreduction system demonstrated the maximum visible-light AQY of 1.07% (at 420 nm) for production of CO. The improved photocatalytic performance was credited to, (i) the compositional features with reduced diffusion length, (ii) hollow morphology, (iii) high specific surface area, (iv) more active sites, and (v) high CO_2 adsorption ability. Thus, excellent features of nanoboxed hierarchical structures led to significantly enhanced photocatalytic activity, which offers a new viewpoint for constructing highly active photocatalysts for visible light-driven CO_2 reduction.

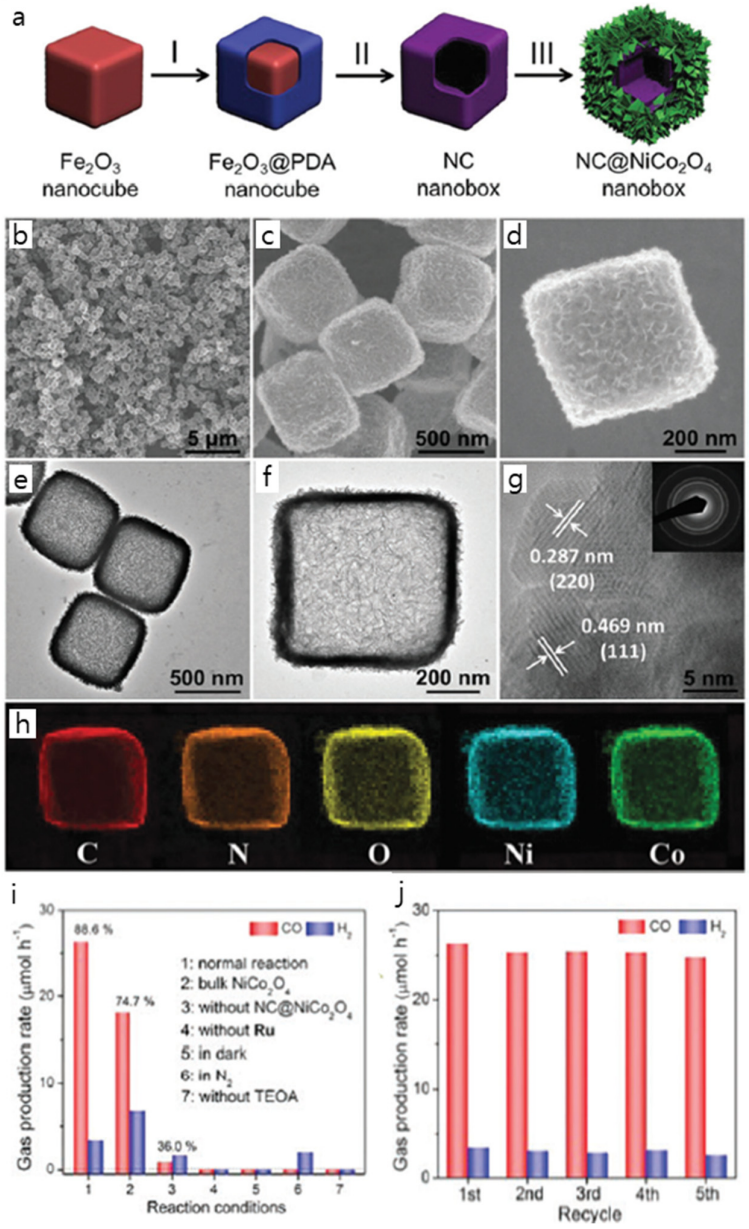

Figure 15. (**a**) Synthetic illustration of NC@$NiCo_2O_4$ of hierarchical nanoboxes, (**b**,**d**) SEM images, (**e**,**f**) TEM images, (**g**) HRTEM with SAED pattern, (**h**) EDX analysis with element mapping, (**i**) The result of the CO_2 reduction test under various conditions and (**j**) stability test of CO and H_2, reprinted with permission from [82].

4.7. Hierarchical Natural Photocatalysts

Sakimoto et al. fabricated a self-augmented biological system by combining the non-photosynthetic bacterium *Moorella thermoacetica* with cadmium sulfide and utilized it for the production of acetic acid [111]. The results showed that, such semi-artificial system undergo CO_2 reduction to produce acetic acid continuously over several days with excellent quantum yield which provides a new route towards CO_2 reduction into useful solar fuels. Therefore, such systems have generated great interest among researchers as an alternative solar-to-fuel CO_2 conversion pathway.

Jiang et al. recently fabricated such a semi-artificial, nature-based visible light-driven hierarchical photocatalyst for CO_2 reduction exhibiting superior activity [112]. In their study, hierarchical treated rape pollen (TRP) was successfully employed for CO_2 photoreduction into CO with yield of 488.4 μmol g^{-1} h^{-1}. Prior to use it for CO_2 photoreduction, the surface of rape pollen was washed

with ethanol and morphology was fixed by treating with ethanol and formaldehyde (1:1) followed by treatment with H_2SO_4 to get final product i.e., TRP. FESEM images revealed its oval shape morphology incorporated with porous network structure (Figure 16a,b).The pore channels in the porous structure were beneficial for maximum light harvesting as shown in Figure 16c. At higher magnification in the TEM images (Figure 16d–f), it can be seen that, the channels are uniformly distributed in porous and hollow structure. However, elemental mapping analysis informed that the TRP is collectively composed of C, O, N and S elements which were further confirmed by XPS. The bandgap of 1.08 eV was calculated by using UV-vis DRS technique. It was observed that, the TRP absorbs light ranging from the UV to visible and NIR region. Therefore all these results confirmed its importance in CO_2 photoreduction reaction. Finally, CO_2 reduction test was carried out at room temperature under irradiation of Xenon lamp (300 W). The results revealed CO was main product of CO_2 reduction along with trace amount of CH_4 formation. Under the full spectrum (i.e., UV-Vis-NIR) the CO evolution rate was 845.7 μmol h^{-1} g^{-1} while under visible light region it was 488.4 μmol h^{-1} g^{-1} (selectivity, 98.3%). It is worth noting that the yield was much higher than common photocatalysts such as P25, g-C_3N_4 and other carbon-based materials at 420 nm along with photostability over three cycles. Such high CO production was attributed to porous and hollow structure containing large surface area of TRP which was further well supported by CO_2 adsorption capacity of 17.2 cm^3 g^{-1}. Therefore, such nature-inspired biomaterials with a unique hierarchical, porous and hollow structure may open a promising avenue for solar light-driven CO_2 photoreduction to produce sustainable solar fuels. Table 2 summarises the latest state of the art CO_2 photoreduction results specifically focussing upon hierarchical nanostructures.

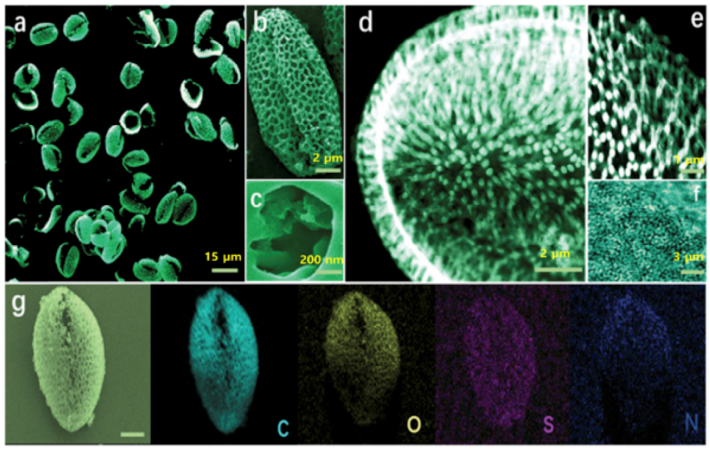

Figure 16. (**a**–**c**) FESEM, (**d**,**e**) HAADF-STEM, (**f**) HRTEM images of TRP particle and (**g**) FESEM image and corresponding elemental mappings of a single TRP particle, reprinted with permission from [112].

In this account, the necessity of solar energy capture for sustainable fuel production has motivated the development of efficient photocatalysts. Hierarchical nanostructures are considered to be potential candidates due to their immense features aimed at conversion of solar energy to chemical energy. Even though various synthetic approaches have been established, it is still challenging to achieve a cost-effective, large-scale fabrication of these hierarchical nanostructures along with high-yield and stability. The state-of-the-art designs for sustainable photocatalysts are always related to the continuous exploitation of fabrication procedures. Therefore, to overcome these issues, discovering novel synthetic approaches could be significant. Refining the current synthesis methods of these hierarchical nanotemplates is also of equal importance. The light scattering phenomenon in the cavities of flower/fruit possess maximum light harvesting ability. For instance, Au@CdS HMCHPs due to its hollow and porous morphology yielded 3758 μmol g^{-1} h^{-1} of CO because of the light-scattering effect. Overall, we believe that the sophisticated hollow and porous structures can provide treasured opportunities in the near future with improvements in cost, yield, processing, and stability.

Table 2. Summary of hierarchical morphologies with specific examples of photocatalysts, CO_2 reduction parameters, and efficiency evaluation of different products along with their yield and apparent quantum yield (AQY).

Hierarchical Morphology	Photocatalyst	Light Source and Reactor Type	CO_2 Photoreduction Results; Yield and AQY	Ref.
Flower-, leaf- and fruit-like structures	Ru-MOF	A 500 W Xe lamp, liquid phase, in a 100 mL Schlenk tube (triethanolamine as a sacrificial agent)	$HCOO^-$, 24.7 μmol g^{-1} (8 h), AQY 0.67%	[89]
	Bi_2MoO_6	A 300 W Xe arc lamp, liquid phase, in closed vessel	CH_3OH, 24.8 and C_2H_5OH, 18.8 μmol g^{-1} (4 h)	[90]
	CeO_2@Bi_2MoO_6	A 300 W Xe arc lamp (PLS-SXE300) with a 420 nm, a closed 200 mL quartz glass reactor containing 50 mL of ultrapure water	CH_3OH and C_2H_5OH, 58.4 μmol g^{-1} (4 h)	[91]
	Perovskite Titanates	A 300 W Xe arc lamp, A gas closed circulation system with an upside window with λ > 420 nm cut-off-filter	CO, 349 and CH_4, 231 nmol g^{-1} h^{-1}	[94]
	Au@CdS HMCHPs (Au, 0.25%)	A 300 W Xe lamp with long-pass cutoff filter, a gas-closed glass reactor (80 mL)	CO, 3758 μmol g^{-1} h^{-1}, AQY, 0.61%	[95]
Spheres (nano/micro)	Pt doped TiO_2 spheres	A 40 W Hg UV lamp, a batch reactor (diameter of 39 mm and depth of 9 mm)	CO, 19 and CH_4, 3.5 μmol g^{-1} h^{-1}, AQY, CO, 1.632% CH_4, 1.315%	[97]
	Porous TiO_2	A 300 W Xe lamp, homemade Pyrex reactor (200 mL)	CH_4, 0.23 μmol h^{-1} and CH_3OH, 0.08 μmol h^{-1}	[98]
	$LaPO_4$	A 125-W high-pressure Hg lamp, Inner-irradiation quartz reactor (200-mL), Liquid phase	CH_4, 10.5 μmol, AQY of 0.54%	[86]
	CdS-WO_3	A 300 W Xe arc lamp with a UV cut-off-filter (λ ≥ 420 nm), home-made Pyrex reactor (200 mL)	CH_4, 1.02 μmol g^{-1} h^{-1}	[99]
	Hollow TiO_2	A non-focused 6 W UV lights (Hitachi F6T5, 365nm), Schlenk flask (80 mL)	CO, 16.8 and H_2, 6.6 μmol (2h), AQY, 0.66%	[100]
Nanofibers	Mesoporous TiO_2	A 6 W UV lamp (λmax = 365 nm), gas-phase stainless steel photoreactor (190 mL)	CO, 203.91, CH_4, 26.88, CH_3OH, 5.04 and H_2, 398.84 μmol g^{-1} AQY, 0.030%	[103]
	TiO_2/$Ni(OH)_2$	A 350 W Xe lamp (40 mW cm^{-2}), self-designed reactor	CH_4, 2.20, CO, 0.71 and CH_3OH, 0.11 μmol g^{-1} h^{-1}	[26]
	2.5% $CuInS_2$/ TiO_2	A 50 W Xe lamp, home-made Pyrex reactor (200 mL)	CH_4, 2.5 and CH_3OH, 0.86 μmol g^{-1} h^{-1}	[104]
	10% MoS_2/TiO_2	A 350 W Xe lamp, home-made reactor	CH_4, 2.86 and CH_3OH, 2.55 μmol g^{-1} h^{-1}, AQY, 0.16%	[105]
Nanotubes	O-g-C_3N_4	A 350 W Xe lamp along with a 420 nm cut-off-filter, Double-neck cylindrical home-made flask (200 mL)	CH_3OH, 0.88 μmol g^{-1} h^{-1}	[87]
	In_2S_3-$CdIn_2S_4$	A 300 W Xe lamp (400 nm cut-off-filter), An 80 mL reactor	CO, 825 μmol h^{-1} g^{-1}	[106]
	$ZnIn_2S_4$-In_2O_3	A 300 W Xe lamp along with a 400 nm cut-off-filter, A 80 mL glass reactor (with gas-closed)	CO, 3075 μmol h^{-1} g^{-1}	[107]
	Bi_2WO_6	A 300 W Xe lamp, A 100 mL quartz reactor	CH_4, 2.6 μmol g^{-1} h^{-1}	[85]
Sheets (and platelets)	ZnV_2O_6	A 35 W HID Xe lamp, A slurry type photoreactor with quartz glass	CH_3OH, 3253.84, HCOOH, 2886.9 and CH_3COOH, 530.1 μmol g^{-1}	[108]
	TiO_2-graphene-MoS_2	A 300 W Xe lamp, stainless-steel reactor	2.33 μmol g^{-1} h^{-1}	[109]
Nanoboxes	N-carbon@$NiCO_2O_4$	A 300W Xe lamp (420 nm cut-off-filter), 80 mL glass reactor	26.2 μmol h^{-1}	[82]
Nature based materials				
Oval	Treated rape pollen	300 W Xenon lamp, closed gas system	CO, 488.4 μmol h^{-1} g^{-1}, Quantum Efficiency (QE), 6.7%	[112]

5. Summary and Outlook

Herein, we have surveyed recent progress in various hierarchical nanostructures with application to CO_2 photoreduction. The use of solar energy for sustainable fuel production has motivated the development of efficient photocatalysts for CO_2 reduction. In conversion of CO_2 reactions efficient adsorption of CO_2 molecule on the surface of photocatalyst is quite important. The high surface area self-assembled hierarchical nanostructured photocatalysts show great potential for promoting CO_2 adsorption due to their abundant active sites and, furthermore, ability to promote enhanced light harvesting. Clearly, advanced fabrication methods affording precise manipulation of surface, structural properties, and a hierarchical pore network are critical for the rational design of high-performance photocatalysts.

Author Contributions: C.H. and S.-I.I. conceptualized, wrote and edited the manuscript. S.A. and S.S. revised the manuscript.

Acknowledgments: The authors gratefully acknowledge the support of the Ministry of Science and ICT (2017R1E1A1A01074890 and 2017M2A2A6A01070912). This research was also supported by the Technology Development Program to Solve Climate Changes of the National Research Foundation (NRF) funded by the Ministry of Science and ICT (2015M1A2A2074670) as well as by the DGIST R&D Program of the Ministry of Science and ICT (19-BD-0404).

Conflicts of Interest: The authors declare no conflict of interest

References

1. Jiang, Z.; Xiao, T.; Kuznetsov, V.L.; Edwards, P.P. Turning carbon dioxide into fuel. *Philos. Trans. Ser. A Math. Phys. Eng. Sci.* **2010**, *368*, 3343–3364. [CrossRef]
2. Zhou, H.; Li, P.; Liu, J.; Chen, Z.; Liu, L.; Dontsova, D.; Yan, R.; Fan, T.; Zhang, D.; Ye, J. Biomimetic polymeric semiconductor based hybrid nanosystems for artificial photosynthesis towards solar fuels generation via CO_2 reduction. *Nano Energy* **2016**, *25*, 128–135. [CrossRef]
3. Tan, L.-L.; Ong, W.-J.; Chai, S.-P.; Mohamed, A.R. Visible-light-activated oxygen-rich TiO_2 as next generation photocatalyst: Importance of annealing temperature on the photoactivity toward reduction of carbon dioxide. *Chem. Eng. J.* **2016**, *283*, 1254–1263. [CrossRef]
4. Shi, Z.; Yang, H.; Gao, P.; Li, X.; Zhong, L.; Wang, H.; Liu, H.; Wei, W.; Sun, Y. Direct conversion of CO_2 to long-chain hydrocarbon fuels over K–promoted CoCu/TiO_2 catalysts. *Catal. Today* **2018**, *311*, 65–73. [CrossRef]
5. Qamar, S.; Lei, F.; Liang, L.; Gao, S.; Liu, K.; Sun, Y.; Ni, W.; Xie, Y. Ultrathin TiO_2 flakes optimizing solar light driven CO_2 reduction. *Nano Energy* **2016**, *26*, 692–698. [CrossRef]
6. Olah, G.A.; Goeppert, A.; Prakash, G.K.S. Chemical recycling of carbon dioxide to methanol and dimethyl ether: From greenhouse gas to renewable, environmentally carbon neutral fuels and synthetic hydrocarbons. *J. Org. Chem.* **2008**, *74*, 487–498. [CrossRef] [PubMed]
7. Low, J.; Cheng, B.; Yu, J. Surface modification and enhanced photocatalytic CO_2 reduction performance of TiO_2: A review. *Appl. Surf. Sci.* **2017**, *392*, 658–686. [CrossRef]
8. Cuéllar-Franca, R.M.; Azapagic, A. Carbon capture, storage and utilisation technologies: A critical analysis and comparison of their life cycle environmental impacts. *J. CO2 Util.* **2015**, *9*, 82–102. [CrossRef]
9. Baldoví, H.G.; Neaţu, S.; Khan, A.; Asiri, A.M.; Kosa, S.A.; Garcia, H. Understanding the origin of the photocatalytic CO_2 reduction by Au-and Cu-loaded TiO_2: A microsecond transient absorption spectroscopy study. *J. Phys. Chem. C* **2015**, *119*, 6819–6827. [CrossRef]
10. Sorcar, S.; Thompson, J.; Hwang, Y.; Park, Y.H.; Majima, T.; Grimes, C.A.; Durrant, J.R.; In, S.-I. High-rate solar-light photoconversion of CO_2 to fuel: Controllable transformation from C1 to C2 products. *Energy Environ. Sci.* **2018**, *11*, 3183–3193. [CrossRef]
11. Marszewski, M.; Cao, S.; Yu, J.; Jaroniec, M. Semiconductor-based photocatalytic CO_2 conversion. *Mater. Horiz.* **2015**, *2*, 261–278. [CrossRef]
12. Li, K.; An, X.; Park, K.H.; Khraisheh, M.; Tang, J. A critical review of CO_2 photoconversion: Catalysts and reactors. *Catal. Today* **2014**, *224*, 3–12. [CrossRef]

13. Taheri Najafabadi, A. CO_2 chemical conversion to useful products: An engineering insight to the latest advances toward sustainability. *Int. J. Energy Res.* **2013**, *37*, 485–499. [CrossRef]
14. Shi, J.; Jiang, Y.; Jiang, Z.; Wang, X.; Wang, X.; Zhang, S.; Han, P.; Yang, C. Enzymatic conversion of carbon dioxide. *Chem. Soc. Rev.* **2015**, *44*, 5981–6000. [CrossRef]
15. Qiao, J.; Liu, Y.; Hong, F.; Zhang, J. A review of catalysts for the electroreduction of carbon dioxide to produce low-carbon fuels. *Chem. Soc. Rev.* **2014**, *43*, 631–675. [CrossRef]
16. Qu, Y.; Duan, X. Progress, challenge and perspective of heterogeneous photocatalysts. *Chem. Soc. Rev.* **2013**, *42*, 2568–2580. [CrossRef] [PubMed]
17. Oh, Y.; Hu, X. Organic molecules as mediators and catalysts for photocatalytic and electrocatalytic CO_2 reduction. *Chem. Soc. Rev.* **2013**, *42*, 2253–2261. [CrossRef]
18. Berardi, S.; Drouet, S.; Francas, L.; Gimbert-Suriñach, C.; Guttentag, M.; Richmond, C.; Stoll, T.; Llobet, A. Molecular artificial photosynthesis. *Chem. Soc. Rev.* **2014**, *43*, 7501–7519. [CrossRef] [PubMed]
19. Chueh, W.C.; Falter, C.; Abbott, M.; Scipio, D.; Furler, P.; Haile, S.M.; Steinfeld, A. High-flux solar-driven thermochemical dissociation of CO_2 and H_2O using nonstoichiometric ceria. *Science* **2010**, *330*, 1797–1801. [CrossRef] [PubMed]
20. Kauffman, D.R.; Thakkar, J.; Siva, R.; Matranga, C.; Ohodnicki, P.R.; Zeng, C.; Jin, R. Efficient electrochemical CO_2 conversion powered by renewable energy. *ACS Appl. Mater. Interfaces* **2015**, *7*, 15626–15632. [CrossRef]
21. Costentin, C.; Robert, M.; Savéant, J.-M. Catalysis of the electrochemical reduction of carbon dioxide. *Chem. Soc. Rev.* **2013**, *42*, 2423–2436. [CrossRef]
22. Benson, E.E.; Kubiak, C.P.; Sathrum, A.J.; Smieja, J.M. Electrocatalytic and homogeneous approaches to conversion of CO_2 to liquid fuels. *Chem. Soc. Rev.* **2009**, *38*, 89–99. [CrossRef] [PubMed]
23. Ganesh, I. Electrochemical conversion of carbon dioxide into renewable fuel chemicals—The role of nanomaterials and the commercialization. *Renew. Sustain. Energy Rev.* **2016**, *59*, 1269–1297. [CrossRef]
24. Olajire, A.A. A review of mineral carbonation technology in sequestration of CO_2. *J. Pet. Sci. Eng.* **2013**, *109*, 364–392. [CrossRef]
25. Walter, M.G.; Warren, E.L.; McKone, J.R.; Boettcher, S.W.; Mi, Q.; Santori, E.A.; Lewis, N.S. Solar water splitting cells. *Chem. Rev.* **2010**, *110*, 6446–6473. [CrossRef]
26. Meng, A.; Wu, S.; Cheng, B.; Yu, J.; Xu, J. Hierarchical TiO_2/$Ni(OH)_2$ composite fibers with enhanced photocatalytic CO_2 reduction performance. *J. Mater. Chem. A* **2018**, *6*, 4729–4736. [CrossRef]
27. Fang, W.; Xing, M.; Zhang, J. Modifications on reduced titanium dioxide photocatalysts: A review. *J. Photochem. Photobiol. C Photochem. Rev.* **2017**, *32*, 21–39. [CrossRef]
28. Inoue, T.; Fujishima, A.; Konishi, S.; Honda, K. Photoelectrocatalytic reduction of carbon dioxide in aqueous suspensions of semiconductor powders. *Nature* **1979**, *277*, 637–638. [CrossRef]
29. Nikokavoura, A.; Trapalis, C. Alternative photocatalysts to TiO_2 for the photocatalytic reduction of CO_2. *Appl. Surf. Sci.* **2017**, *391*, 149–174. [CrossRef]
30. Yu, J.; Wang, K.; Xiao, W.; Cheng, B. Photocatalytic reduction of CO_2 into hydrocarbon solar fuels over gC_3N_4–Pt nanocomposite photocatalysts. *Phys. Chem. Chem. Phys.* **2014**, *16*, 11492–11501. [CrossRef] [PubMed]
31. Reli, M.; Kobielusz, M.; Daniš, S.; Macyk, W.; Obalová, L.; Kuśtrowski, P.; Rokicińska, A.; Kočí, K. TiO_2 Processed by pressurized hot solvents as a novel photocatalyst for photocatalytic reduction of carbon dioxide. *Appl. Surf. Sci.* **2017**, *391*, 282–287. [CrossRef]
32. Yan, S.; Ouyang, S.; Xu, H.; Zhao, M.; Zhang, X.; Ye, J. Co-ZIF-9/TiO_2 nanostructure for superior CO_2 photoreduction activity. *J. Mater. Chem. A* **2016**, *4*, 15126–15133. [CrossRef]
33. Yu, J.; Jin, J.; Cheng, B.; Jaroniec, M. A noble metal-free reduced graphene oxide–CdS nanorod composite for the enhanced visible-light photocatalytic reduction of CO_2 to solar fuel. *J. Mater. Chem. A* **2014**, *2*, 3407–3416. [CrossRef]
34. Meng, A.; Zhu, B.; Zhong, B.; Zhang, L.; Cheng, B. Direct Z-scheme TiO_2/CdS hierarchical photocatalyst for enhanced photocatalytic H_2-production activity. *Appl. Surf. Sci.* **2017**, *422*, 518–527. [CrossRef]
35. Yu, W.; Zhang, J.; Peng, T. New insight into the enhanced photocatalytic activity of N-, C-and S-doped ZnO photocatalysts. *Appl. Catal. B Environ.* **2016**, *181*, 220–227. [CrossRef]
36. Yu, W.; Chen, J.; Shang, T.; Chen, L.; Gu, L.; Peng, T. Direct Z-scheme g-C_3N_4/WO_3 photocatalyst with atomically defined junction for H_2 production. *Appl. Catal. B Environ.* **2017**, *219*, 693–704. [CrossRef]

37. Akple, M.S.; Low, J.; Qin, Z.; Wageh, S.; Al-Ghamdi, A.A.; Yu, J.; Liu, S. Nitrogen-doped TiO_2 microsheets with enhanced visible light photocatalytic activity for CO_2 reduction. *Chin. J. Catal.* **2015**, *36*, 2127–2134. [CrossRef]
38. Low, J.; Yu, J.; Ho, W. Graphene-based photocatalysts for CO_2 reduction to solar fuel. *J. Phys. Chem. Lett.* **2015**, *6*, 4244–4251. [CrossRef] [PubMed]
39. Kim, K.; Razzaq, A.; Sorcar, S.; Park, Y.; Grimes, C.A.; In, S.-I. Hybrid mesoporous Cu_2ZnSnS_4 (CZTS)–TiO_2 photocatalyst for efficient photocatalytic conversion of CO_2 into CH_4 under solar irradiation. *RSC Adv.* **2016**, *6*, 38964–38971. [CrossRef]
40. Sorcar, S.; Hwang, Y.; Grimes, C.A.; In, S.-I. Highly enhanced and stable activity of defect-induced titania nanoparticles for solar light-driven CO_2 reduction into CH_4. *Mater. Today* **2017**, *20*, 507–515. [CrossRef]
41. Tjandra, A.D.; Huang, J. Photocatalytic carbon dioxide reduction by photocatalyst innovation. *Chin. Chem. Lett.* **2018**, *31*, 734–746. [CrossRef]
42. Grills, D.C.; Fujita, E. New directions for the photocatalytic reduction of CO_2: Supramolecular, $scCO_2$ or biphasic ionic liquid−$scCO_2$ systems. *J. Phys. Chem. Lett.* **2010**, *1*, 2709–2718. [CrossRef]
43. Liu, L.; Zhao, C.; Li, Y. Spontaneous dissociation of CO_2 to CO on defective surface of Cu(I)/TiO_{2-x} nanoparticles at room temperature. *J. Phys. Chem. C* **2012**, *116*, 7904–7912. [CrossRef]
44. Corma, A.; Garcia, H. Photocatalytic reduction of CO_2 for fuel production: Possibilities and challenges. *J. Catal.* **2013**, *308*, 168–175. [CrossRef]
45. Sato, S.; Arai, T.; Morikawa, T. Toward solar-driven photocatalytic CO_2 reduction using water as an electron donor. *Inorg. Chem.* **2015**, *54*, 5105–5113. [CrossRef]
46. Anpo, M. Photocatalytic reduction of CO_2 with H_2O on highly dispersed Ti-oxide catalysts as a model of artificial photosynthesis. *J. CO2 Util.* **2013**, *1*, 8–17. [CrossRef]
47. Li, K.; Peng, B.; Peng, T. Recent advances in heterogeneous photocatalytic CO_2 conversion to solar fuels. *ACS Catal.* **2016**, *6*, 7485–7527. [CrossRef]
48. Habisreutinger, S.N.; Schmidt-Mende, L.; Stolarczyk, J.K. Photocatalytic reduction of CO_2 on TiO_2 and other semiconductors. *Angew. Chem. Int. Ed.* **2013**, *52*, 7372–7408. [CrossRef]
49. Xin, C.; Hu, M.; Wang, K.; Wang, X. Significant enhancement of photocatalytic reduction of CO_2 with H_2O over ZnO by the formation of basic zinc carbonate. *Langmuir* **2017**, *33*, 6667–6676. [CrossRef]
50. Liu, X.; Ye, L.; Liu, S.; Li, Y.; Ji, X. Photocatalytic reduction of CO_2 by ZnO micro/nanomaterials with different morphologies and ratios of {0001} facets. *Sci. Rep.* **2016**, *6*, 38474. [CrossRef] [PubMed]
51. Zhang, L.; Li, N.; Jiu, H.; Qi, G.; Huang, Y. ZnO-reduced graphene oxide nanocomposites as efficient photocatalysts for photocatalytic reduction of CO_2. *Ceram. Int.* **2015**, *41*, 6256–6262. [CrossRef]
52. Xu, Q.; Yu, J.; Zhang, J.; Zhang, J.; Liu, G. Cubic anatase TiO_2 nanocrystals with enhanced photocatalytic CO_2 reduction activity. *Chem. Commun.* **2015**, *51*, 7950–7953. [CrossRef]
53. Sim, L.C.; Leong, K.H.; Saravanan, P.; Ibrahim, S. Rapid thermal reduced graphene oxide/Pt–TiO_2 nanotube arrays for enhanced visible-light-driven photocatalytic reduction of CO_2. *Appl. Surf. Sci.* **2015**, *358*, 122–129. [CrossRef]
54. Li, Y.; Wang, W.-N.; Zhan, Z.; Woo, M.-H.; Wu, C.-Y.; Biswas, P. Photocatalytic reduction of CO_2 with H_2O on mesoporous silica supported Cu/TiO_2 catalysts. *Appl. Catal. B Environ.* **2010**, *100*, 386–392. [CrossRef]
55. Wang, T.; Meng, X.; Li, P.; Ouyang, S.; Chang, K.; Liu, G.; Mei, Z.; Ye, J. Photoreduction of CO_2 over the well-crystallized ordered mesoporous TiO_2 with the confined space effect. *Nano Energy* **2014**, *9*, 50–60. [CrossRef]
56. Wang, L.; Sasaki, T. Titanium oxide nanosheets: Graphene analogues with versatile functionalities. *Chem. Rev.* **2014**, *114*, 9455–9486. [CrossRef]
57. Kar, P.; Zeng, S.; Zhang, Y.; Vahidzadeh, E.; Manuel, A.; Kisslinger, R.; Alam, K.M.; Thakur, U.K.; Mahdi, N.; Kumar, P. High rate CO_2 photoreduction using flame annealed TiO_2 nanotubes. *Appl. Catal. B Environ.* **2019**, *243*, 522–536. [CrossRef]
58. Fang, W.; Khrouz, L.; Zhou, Y.; Shen, B.; Dong, C.; Xing, M.; Mishra, S.; Daniele, S.; Zhang, J. Reduced {001}-TiO_{2-x} photocatalysts: Noble-metal-free CO_2 photoreduction for selective CH_4 evolution. *Phys. Chem. Chem. Phys.* **2017**, *19*, 13875–13881. [CrossRef]
59. Ijaz, S.; Ehsan, M.F.; Ashiq, M.N.; Karamat, N.; He, T. Preparation of CdS@CeO_2 core/shell composite for photocatalytic reduction of CO_2 under visible-light irradiation. *Appl. Surf. Sci.* **2016**, *390*, 550–559. [CrossRef]

60. Cho, K.M.; Kim, K.H.; Park, K.; Kim, C.; Kim, S.; Al-Saggaf, A.; Gereige, I.; Jung, H.-T. Amine-functionalized graphene/CdS composite for photocatalytic reduction of CO_2. *ACS Catal.* **2017**, *7*, 7064–7069. [CrossRef]
61. Yang, X.; Xin, W.; Yin, X.; Shao, X. Syntheses and evaluations of CdS with various morphologies for photocatalytically reducing CO_2. *J. Wuhan Univ. Technol. Sci. Ed.* **2018**, *33*, 78–84. [CrossRef]
62. Wang, J.-C.; Zhang, L.; Fang, W.-X.; Ren, J.; Li, Y.-Y.; Yao, H.-C.; Wang, J.-S.; Li, Z.-J. Enhanced photoreduction CO_2 activity over direct Z-scheme α-Fe_2O_3/Cu_2O heterostructures under visible light irradiation. *ACS Appl. Mater. Interfaces* **2015**, *7*, 8631–8639. [CrossRef] [PubMed]
63. Li, P.; Jing, H.; Xu, J.; Wu, C.; Peng, H.; Lu, J.; Lu, F. High-efficiency synergistic conversion of CO_2 to methanol using Fe_2O_3 nanotubes modified with double-layer Cu_2O spheres. *Nanoscale* **2014**, *6*, 11380–11386. [CrossRef] [PubMed]
64. Wang, J.; Liu, H.; Xu, Y.; Zhang, X. Preparation of Fe_2O_3-TiO_2 and its photocatalytic reduction of CO_2 to methanol. *Asian J. Chem.* **2014**, *26*, 3875–3878. [CrossRef]
65. Sun, Z.; Wang, H.; Wu, Z.; Wang, L. g-C_3N_4 based composite photocatalysts for photocatalytic CO_2 reduction. *Catal. Today* **2018**, *300*, 160–172. [CrossRef]
66. Tang, J.; Zhou, W.; Guo, R.; Huang, C.; Pan, W. Enhancement of photocatalytic performance in CO_2 reduction over Mg/g-C_3N_4 catalysts under visible light irradiation. *Catal. Commun.* **2018**, *107*, 92–95. [CrossRef]
67. Ye, L.; Wu, D.; Chu, K.H.; Wang, B.; Xie, H.; Yip, H.Y.; Wong, P.K. Phosphorylation of g-C_3N_4 for enhanced photocatalytic CO_2 reduction. *Chem. Eng. J.* **2016**, *304*, 376–383. [CrossRef]
68. Ong, W.-J.; Tan, L.-L.; Chai, S.-P.; Yong, S.-T.; Mohamed, A.R. Surface charge modification via protonation of graphitic carbon nitride (g-C_3N_4) for electrostatic self-assembly construction of 2D/2D reduced graphene oxide (rGO)/g-C_3N_4 nanostructures toward enhanced photocatalytic reduction of carbon dioxide to methane. *Nano Energy* **2015**, *13*, 757–770. [CrossRef]
69. Wang, K.; Li, Q.; Liu, B.; Cheng, B.; Ho, W.; Yu, J. Sulfur-doped g-C_3N_4 with enhanced photocatalytic CO_2-reduction performance. *Appl. Catal. B Environ.* **2015**, *176*, 44–52. [CrossRef]
70. Li, F.; Zhang, L.; Tong, J.; Liu, Y.; Xu, S.; Cao, Y.; Cao, S. Photocatalytic CO_2 conversion to methanol by Cu_2O/graphene/TNA heterostructure catalyst in a visible-light-driven dual-chamber reactor. *Nano Energy* **2016**, *27*, 320–329. [CrossRef]
71. Xu, H.; Ouyang, S.; Liu, L.; Wang, D.; Kako, T.; Ye, J. Porous-structured Cu_2O/TiO_2 nanojunction material toward efficient CO_2 photoreduction. *Nanotechnology* **2014**, *25*, 165402. [CrossRef] [PubMed]
72. An, X.; Li, K.; Tang, J. Cu_2O/reduced graphene oxide composites for the photocatalytic conversion of CO_2. *ChemSusChem* **2014**, *7*, 1086–1093. [CrossRef]
73. Murcia-López, S.; Vaiano, V.; Hidalgo, M.C.; Navío, J.A.; Sannino, D. Photocatalytic reduction of CO_2 over platinised Bi_2WO_6-based materials. *Photochem. Photobiol. Sci.* **2015**, *14*, 678–685. [CrossRef] [PubMed]
74. Sun, Z.; Yang, Z.; Liu, H.; Wang, H.; Wu, Z. Visible-light CO_2 photocatalytic reduction performance of ball-flower-like Bi_2WO_6 synthesized without organic precursor: Effect of post-calcination and water vapor. *Appl. Surf. Sci.* **2014**, *315*, 360–367. [CrossRef]
75. Kong, X.Y.; Choo, Y.Y.; Chai, S.-P.; Soh, A.K.; Mohamed, A.R. Oxygen vacancy induced Bi_2WO_6 for the realization of photocatalytic CO_2 reduction over the full solar spectrum: From the UV to the NIR region. *Chem. Commun.* **2016**, *52*, 14242–14245. [CrossRef] [PubMed]
76. Li, X.; Yu, J.; Jaroniec, M. Hierarchical photocatalysts. *Chem. Soc. Rev.* **2016**, *45*, 2603–2636. [CrossRef] [PubMed]
77. Zhou, P.; Yu, J.; Jaroniec, M. All-solid-state Z-scheme photocatalytic systems. *Adv. Mater.* **2014**, *26*, 4920–4935. [CrossRef] [PubMed]
78. Li, P.; Ouyang, S.; Xi, G.; Kako, T.; Ye, J. The effects of crystal structure and electronic structure on photocatalytic H_2 evolution and CO_2 reduction over two phases of perovskite-structured $NaNbO_3$. *J. Phys. Chem. C* **2012**, *116*, 7621–7628. [CrossRef]
79. Iizuka, K.; Wato, T.; Miseki, Y.; Saito, K.; Kudo, A. Photocatalytic reduction of carbon dioxide over Ag cocatalyst-loaded $ALa_4Ti_4O_{15}$ (A= Ca, Sr, and Ba) using water as a reducing reagent. *J. Am. Chem. Soc.* **2011**, *133*, 20863–20868. [CrossRef] [PubMed]
80. Fang, M.; Dong, G.; Wei, R.; Ho, J.C. Hierarchical nanostructures: Design for sustainable water splitting. *Adv. Energy Mater.* **2017**, *7*, 1700559. [CrossRef]
81. Gao, X.; Li, G.; Xu, Y.; Hong, Z.; Liang, C.; Lin, Z. TiO_2 Microboxes with controlled internal porosity for high-performance lithium storage. *Angew. Chem. Int. Ed.* **2015**, *54*, 14331–14335. [CrossRef]

82. Wang, S.; Guan, B.Y.; Lou, X.W.D. Rationally designed hierarchical N-doped carbon@$NiCo_2O_4$ double-shelled nanoboxes for enhanced visible light CO_2 reduction. *Energy Environ. Sci.* **2018**, *11*, 306–310. [CrossRef]
83. Ali, S.; Razzaq, A.; In, S.-I. Development of graphene based photocatalysts for CO_2 reduction to C1 chemicals: A brief overview. *Catal. Today* **2018**. [CrossRef]
84. Jiao, W.; Wang, L.; Liu, G.; Lu, G.Q.; Cheng, H.-M. Hollow anatase TiO_2 single crystals and mesocrystals with dominant {101} facets for improved photocatalysis activity and tuned reaction preference. *ACS Catal.* **2012**, *2*, 1854–1859. [CrossRef]
85. Xiao, L.; Lin, R.; Wang, J.; Cui, C.; Wang, J.; Li, Z. A novel hollow-hierarchical structured Bi_2WO_6 with enhanced photocatalytic activity for CO_2 photoreduction. *J. Colloid Interface Sci.* **2018**, *523*, 151–158. [CrossRef]
86. Pan, B.; Zhou, Y.; Su, W.; Wang, X. Self-assembly synthesis of $LaPO_4$ hierarchical hollow spheres with enhanced photocatalytic CO_2-reduction performance. *Nano Res.* **2017**, *10*, 534–545. [CrossRef]
87. Fu, J.; Zhu, B.; Jiang, C.; Cheng, B.; You, W.; Yu, J. Hierarchical porous O-doped g-C_3N_4 with enhanced photocatalytic CO_2 reduction activity. *Small* **2017**, *13*, 1603938. [CrossRef] [PubMed]
88. Wang, X.; Yu, J.C.; Ho, C.; Hou, Y.; Fu, X. Photocatalytic activity of a hierarchically macro/mesoporous titania. *Langmuir* **2005**, *21*, 2552–2559. [CrossRef] [PubMed]
89. Sun, J.; Zhang, J.; Zhang, M.; Antonietti, M.; Fu, X.; Wang, X. Bioinspired hollow semiconductor nanospheres as photosynthetic nanoparticles. *Nat. Commun.* **2012**, *3*, 1139. [CrossRef]
90. Hailili, R.; Jacobs, D.L.; Zang, L.; Wang, C. Morphology controlled synthesis of $CeTiO_4$ using molten salts and enhanced photocatalytic activity for CO_2 reduction. *Appl. Surf. Sci.* **2018**, *456*, 360–368. [CrossRef]
91. Zhang, S.; Li, L.; Zhao, S.; Sun, Z.; Hong, M.; Luo, J. Hierarchical metal-organic framework nanoflowers for effective CO_2 transformation driven by visible light. *J. Mater. Chem. A* **2015**, *3*, 15764–15768. [CrossRef]
92. Dai, W.; Yu, J.; Xu, H.; Hu, X.; Luo, X.; Yang, L.; Tu, X. Synthesis of hierarchical flower-like Bi_2MoO_6 microspheres as efficient photocatalyst for photoreduction of CO_2 into solar fuels under visible light. *CrystEngComm* **2016**, *18*, 3472–3480. [CrossRef]
93. Dai, W.; Hu, X.; Wang, T.; Xiong, W.; Luo, X.; Zou, J. Hierarchical CeO_2/Bi_2MoO_6 heterostructured nanocomposites for photoreduction of CO_2 into hydrocarbons under visible light irradiation. *Appl. Surf. Sci.* **2018**, *434*, 481–491. [CrossRef]
94. Zhou, H.; Guo, J.; Li, P.; Fan, T.; Zhang, D.; Ye, J. Leaf-architectured 3D hierarchical artificial photosynthetic system of perovskite titanates towards CO_2 photoreduction into hydrocarbon fuels. *Sci. Rep.* **2013**, *3*, 1667. [CrossRef] [PubMed]
95. Zhang, P.; Wang, S.; Guan, B.Y.; Lou, X.W.D. Fabrication of CdS hierarchical multi-cavity hollow particles for efficient visible light CO_2 reduction. *Energy Environ. Sci.* **2019**, *12*, 164–168. [CrossRef]
96. Wang, Y.; Zhang, L.; Zhang, X.; Zhang, Z.; Tong, Y.; Li, F.; Wu, J.C.-S.; Wang, X. Openmouthed β-SiC hollow-sphere with highly photocatalytic activity for reduction of CO_2 with H_2O. *Appl. Catal. B Environ.* **2017**, *206*, 158–167. [CrossRef]
97. Fang, B.; Bonakdarpour, A.; Reilly, K.; Xing, Y.; Taghipour, F.; Wilkinson, D.P. Large-scale synthesis of TiO_2 microspheres with hierarchical nanostructure for highly efficient photodriven reduction of CO_2 to CH_4. *ACS Appl. Mater. Interfaces* **2014**, *6*, 15488–15498. [CrossRef] [PubMed]
98. Di, T.; Zhang, J.; Cheng, B.; Yu, J.; Xu, J. Hierarchically nanostructured porous TiO_2(B) with superior photocatalytic CO_2 reduction activity. *Sci. China Chem.* **2018**, *61*, 344–350. [CrossRef]
99. Jin, J.; Yu, J.; Guo, D.; Cui, C.; Ho, W. A Hierarchical Z-scheme CdS–WO_3 photocatalyst with enhanced CO_2 reduction activity. *Small* **2015**, *11*, 5262–5271. [CrossRef] [PubMed]
100. Lin, J.; Sun, X.; Qin, B.; Yu, T. Improving the photocatalytic reduction of CO_2 to CO for TiO_2 hollow spheres through hybridization with a cobalt complex. *RSC Adv.* **2018**, *8*, 20543–20548. [CrossRef]
101. Wu, H.; Kong, D.; Ruan, Z.; Hsu, P.-C.; Wang, S.; Yu, Z.; Carney, T.J.; Hu, L.; Fan, S.; Cui, Y. A transparent electrode based on a metal nanotrough network. *Nat. Nanotechnol.* **2013**, *8*, 421–425. [CrossRef] [PubMed]
102. Le, V.T.; Kim, H.; Ghosh, A.; Kim, J.; Chang, J.; Vu, Q.A.; Pham, D.T.; Lee, J.-H.; Kim, S.-W.; Lee, Y.H. Coaxial fiber supercapacitor using all-carbon material electrodes. *ACS Nano* **2013**, *7*, 5940–5947. [CrossRef]
103. Reñones, P.; Moya, A.; Fresno, F.; Collado, L.; Vilatela, J.J.; Víctor, A. Hierarchical TiO_2 nanofibres as photocatalyst for CO_2 reduction: Influence of morphology and phase composition on catalytic activity. *J. CO2 Util.* **2016**, *15*, 24–31. [CrossRef]
104. Xu, F.; Zhang, J.; Zhu, B.; Yu, J.; Xu, J. $CuInS_2$ sensitized TiO_2 hybrid nanofibers for improved photocatalytic CO_2 reduction. *Appl. Catal. B Environ.* **2018**, *230*, 194–202. [CrossRef]

105. Xu, F.; Zhu, B.; Cheng, B.; Yu, J.; Xu, J. 1D/2D TiO_2/MoS_2 hybrid nanostructures for enhanced photocatalytic CO_2 reduction. *Adv. Opt. Mater.* **2018**, *6*, 1800911. [CrossRef]
106. Wang, S.; Guan, B.Y.; Lu, Y.; Lou, X.W. Formation of hierarchical In_2S_3–$CdIn_2S_4$ heterostructured nanotubes for efficient and stable visible light CO_2 reduction. *J. Am. Chem. Soc.* **2017**, *139*, 17305–17308. [CrossRef]
107. Wang, S.; Guan, B.Y.; Lou, X.W.D. Construction of $ZnIn_2S_4$–In_2O_3 hierarchical tubular heterostructures for efficient CO_2 photoreduction. *J. Am. Chem. Soc.* **2018**, *140*, 5037–5040. [CrossRef]
108. Bafaqeer, A.; Tahir, M.; Amin, N.A.S. Synthesis of hierarchical ZnV_2O_6 nanosheets with enhanced activity and stability for visible light driven CO_2 reduction to solar fuels. *Appl. Surf. Sci.* **2018**, *435*, 953–962. [CrossRef]
109. Jung, H.; Cho, K.M.; Kim, K.H.; Yoo, H.-W.; Al-Saggaf, A.; Gereige, I.; Jung, H.-T. Highly efficient and stable CO_2 reduction photocatalyst with a hierarchical structure of mesoporous TiO_2 on 3D graphene with few-layered MoS_2. *ACS Sustain. Chem. Eng.* **2018**, *6*, 5718–5724. [CrossRef]
110. Qiu, B.; Zhu, Q.; Du, M.; Fan, L.; Xing, M.; Zhang, J. Efficient solar light harvesting CdS/Co_9S_8 hollow cubes for Z-Scheme photocatalytic water splitting. *Angew. Chem. Int. Ed.* **2017**, *56*, 2684–2688. [CrossRef]
111. Sakimoto, K.K.; Wong, A.B.; Yang, P. Self-photosensitization of nonphotosynthetic bacteria for solar-to-chemical production. *Science* **2016**, *351*, 74–77. [CrossRef] [PubMed]
112. Jiang, Z.; Sun, H.; Wang, T.; Wang, B.; Wei, W.; Li, H.; Yuan, S.; An, T.; Zhao, H.; Yu, J. Nature-based catalyst for visible-light-driven photocatalytic CO_2 reduction. *Energy Environ. Sci.* **2018**, *11*, 2382–2389. [CrossRef]